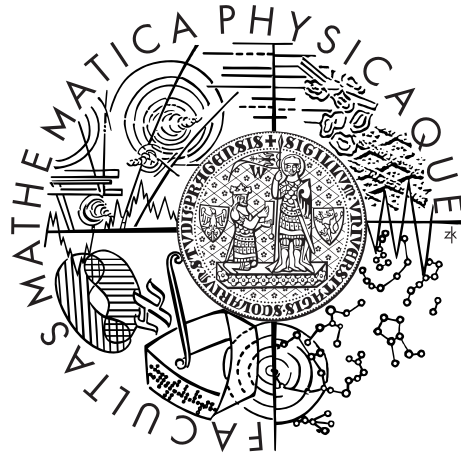Charles University in Prague
Faculty of Mathematics and Physics

BACHELOR THESIS

Radek Zajíček

Transport Between the Stratosphere and Mesosphere

Department of Atmospheric Physics

Supervisor of the bachelor thesis: Doc. RNDr. Petr Pišoft, Ph.D.
Study programme: General Physics

Prague 2021

I declare that I carried out this bachelor thesis independently, and only with the cited sources, literature and other professional sources.

I understand that my work relates to the rights and obligations under the Act No. 121/2000 Coll., the Copyright Act, as amended, in particular the fact that the Charles University in Prague has the right to conclude a license agreement on the use of this work as a school work pursuant to Section 60 paragraph 1 of the Copyright Act.

In . . . . on . . . .   Author signature

Název práce: Transport mezi stratosférou a mezosférou

Autor: Radek Zajíček

Katedra: Katedra fyziky atmosféry

Vedoucí bakalářské práce: Doc. RNDr. Petr Pišoft, Ph.D., Katedra fyziky atmosféry

Abstrakt: Transport mezi stratosférou a mezosférou je řízen velkoprostorou Brewer-Dobsonovou cirkulací. V této práci je zkoumán vliv skleníkových plynů a ozon narušujících látek na vývoj vertikálního toku ve střední atmosféře pro období 1960-2080, zejména pak integrovaných toků skrz stratopauzu. Analýza vertikálního toku je založena na reziduální proudové funkci, jejíž data byla získána výpočtem z chemicko-klimatických modelů v rámci iniciativy CCMI-1 (Chemistry–Climate Model Initiative). Výsledky práce ukazují na jednoznačný vliv rostoucích koncentrací skleníkových plynů v atmosféře na zesílení hluboké větve Brewer-Dobsonovy cirkulace a to jak ve vzestupných, tak také sestupných pohybech.

Klíčová slova: stratosféra, mezosféra, Brewerova-Dobsonova cirkulace

Title: Transport between the stratosphere and mesosphere

Author: Radek Zajíček

Department: Department of Atmospheric Physics

Supervisor of the bachelor thesis: Doc. RNDr. Petr Pišoft, Ph.D., Department of Atmospheric Physics

Abstract: The transport between the stratosphere and mesosphere is controlled by the large-scale Brewer-Dobson circulation. This thesis investigates the influence of greenhouse gases and ozone-depleting substances on the development of vertical flow in the middle atmosphere for the period 1960-2080, especially integrated flows through the stratopause. The vertical flow analysis is based on the residual stream function, the data of which were obtained by calculation from chemistry–climate models within the Chemistry–Climate Model Initiative (CCMI-1) . The results of the work show a clear effect of increasing concentration of greenhouse gases in the atmosphere on the amplification of the deep branch of the Brewer-Dobson circulation, both in ascending and descending movements.

Keywords: stratosphere, mesosphere, Brewer-Dobson circulation

Contents

Introduction

The atmosphere can be divided into layers according to the vertical temperature gradient. The presented analysis focuses on the circulation within the middle atmosphere defined as a region from the tropopause to the homopause (about 10–110 km), including the stratosphere, mesosphere, and lower thermosphere (Andrews et al., 1987). The study presents an analysis of the transport between the stratosphere and mesosphere, focusing on the future evolution simulated by the chemistry-climate models.

The atmospheric layers are coupled by various processes among which the vertical circulation, i.e. the Brewer-Dobson circulation, plays a principal role. It vertically transports atmospheric gasses, including constituents like ozone, green house gasses or chemical families important for the ozone destruction reactions. The circulation is influenced by the climate change and it also provides a feedback to the climate change related trends.

The study is based on analysis of the chemistry-climate models, namely, the models included in the Chemistry Climate Models Initiative - CCMI (Morgenstern et al., 2017). We have analyzed all forcing scenario and two sensitivity experiments, one with fixed ozone-depleting substances and the other one with fixed greenhouse gases, for the 1960-2080 period.

Our results show a distinct trend linked to the changes in the upper part of the Brewer-Dobson circulation. The models' simulation shows that there is increasing tropical upwelling and increasing seasonal downwelling over middle and high latitudes. The analysis of the sensitivity simulations indicates that the detected trends might be attributed mainly to the increasing concentration of green house gases.

The thesis is structured as follows. The first chapter generally introduces the atmospheric composition and vertical structure. The second chapter describes basics of the middle atmospheric climatology and circulation. Furthermore, it highlights specifics of the Brewer-Dobson circulation. The model data and methodology are introduced in the following chapter. The fourth chapter presents the results that are discussed in the last chapter.

Chapter 1

Atmospheric Structure

1.1 Vertical Stratification of the Atmosphere

There are multiple ways to divide the atmosphere vertically. It can be divided, e.g., into two layers according to the homogeneity of the composition. The first, in which gases are well mixed, is called the homosphere. It reaches a height of about 100 km above the Earth's surface (Mohanakumar, 2008). Above the homosphere, there is a stratum called the heterosphere with a predominance of molecular diffusion over eddy dispersion. Lack of turbulence mixing leads to a separation of gases according to their mass so that the density of the heavier molecules decreases with the altitude faster than for the lighter ones. Exceptions to the homogeneous distribution of gases in the homosphere are water vapour and ozone, which have a specific and highly variable distribution. The division of the atmosphere according to its composition's homogeneity is important for specific studies. However, the best known and most utilised is the classification associated with changes in the vertical gradient of temperature.

1.1.1 Temperature-based Division

Based on changes in the vertical temperature profile, the atmosphere is divided into layers called spheres (see Fig. 1.1). The boundaries between these layers are marked as pauses. A sphere is a concentric stratum where the temperature changes monotonically with altitude, and pauses are strata where the temperature gradient changes its sign.

The lowest layer is called the troposphere, characterised by a decrease in temperature with increasing altitude. The average drop is around 6-8 °C/km (Mohanakumar, 2008) and is greatly affected by the amount of water vapour, which is typical for the troposphere. The water vapour absorbs solar energy and thermal radiation from the Earth's surface. Unsurprisingly, water vapour concentration also decreases with altitude and is strongly dependent on latitude; it is the highest above the equator and decreases towards the poles. The thickness of the troposphere varies between 8 and 18 kilometres (300-100 hPa), depending on latitude with the maximal height around the equator (Fig. 1.2).
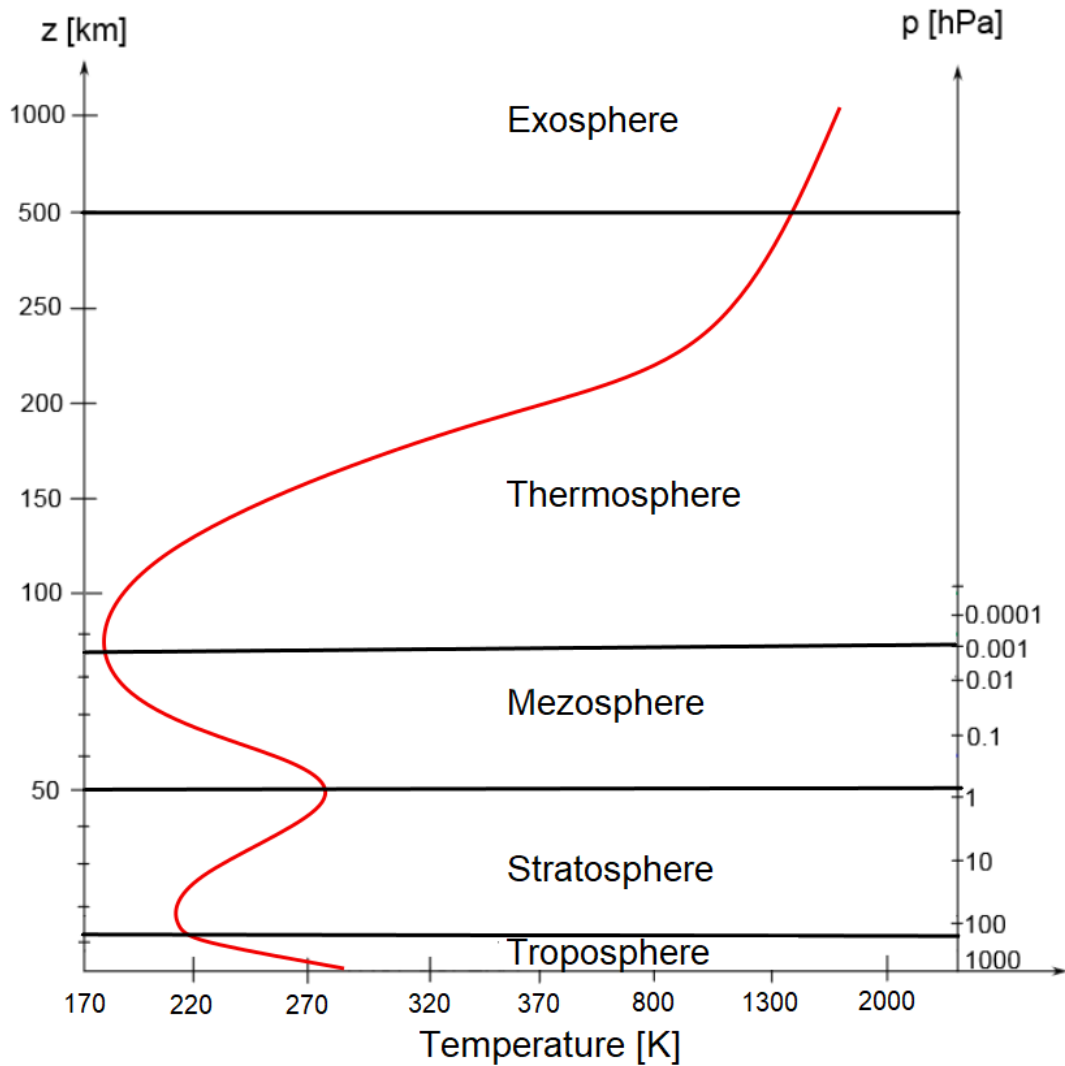
Figure 1.1: Scheme of vertical division of the atmosphere according to the temperature profile.

Between the troposphere and the next layer, called the stratosphere, is a transition zone termed the tropopause. The tropopause is defined as a stratum with the temperature drop below 0.2 °C/km (WMO, 1957). The equatorial tropopause is the coldest part of the lower 20 kilometres of the atmosphere. Towards the poles, the tropopause is warmer (Fig. 1.2). As the stratosphere inhibits vertical mixing, there are significant concentration gradients in the tropopause, especially the concentration of water vapour and ozone differs considerably between the troposphere and the stratosphere. The stratosphere reaches a height of about 50 kilometres (1 hPa), where the stratopause is located. Unlike the troposphere, the temperature in the stratosphere rises with altitude. This is due to the increasing concentration of ozone molecules that absorb UV radiation, leading to higher temperatures. Thus, the stratosphere is very stable with minimal vertical air mixing. Compared to the troposphere, the concentration of water vapour in the stratosphere is low. Hence, clouds are rather exceptional here.
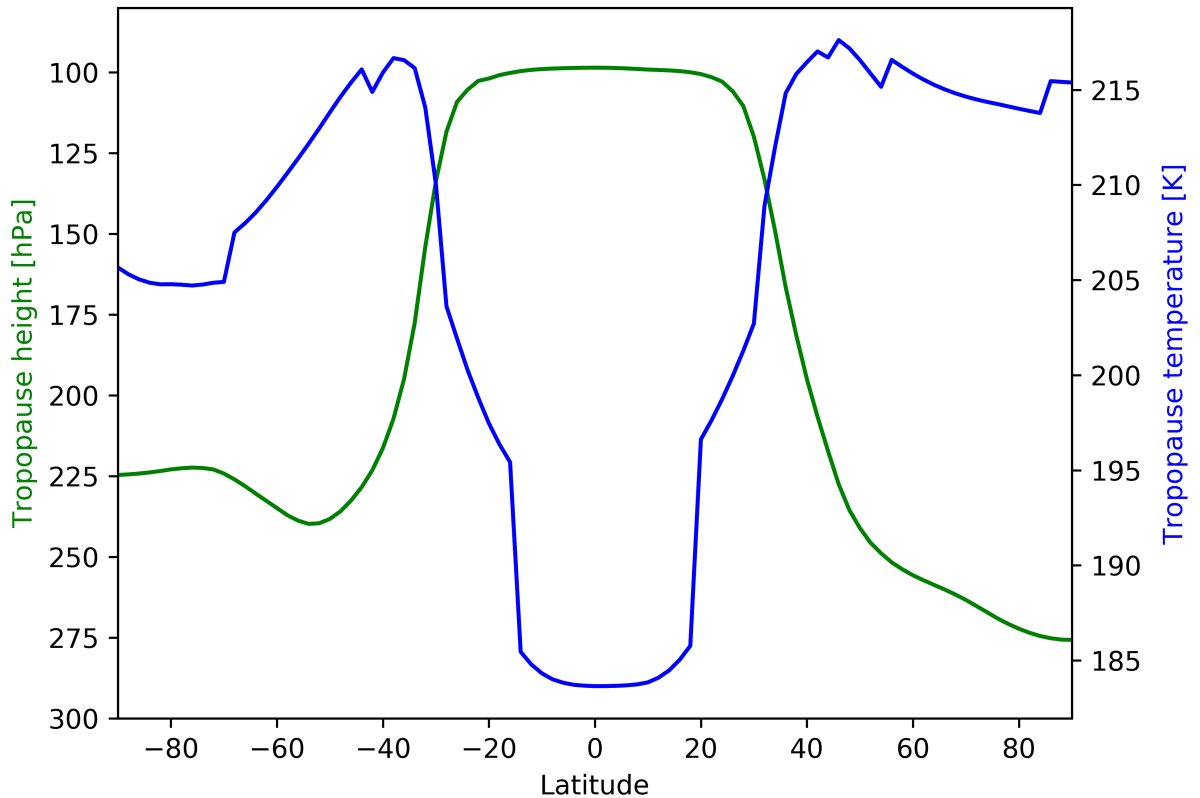
Figure 1.2: Tropopause annual mean height and temperature from the chemistry-climate model CMAM REF-C2 scenario for 1960-2000.

The third primary stratum, extending from 50 to 80 km (1-0.01 hPa), is called the mesosphere. The ozone concentration is very low here. Therefore, the heat from the absorbing UV radiation is negligible, and the temperature decreases with altitude. The mesosphere is bounded from above by the mesopause, where the temperature drops down to 150 K.

In the thermosphere, the temperature starts growing rapidly with altitude to 500-2000 K. Since the thermosphere belongs to the heterosphere, the chemical composition is different from the lower layers. The concentration of atomic oxygen here increases with height, hence the high temperatures. The temperature rise stops, depending on the level of solar radiation, at an altitude between 250 and 500 kilometres, and we call this region the thermopause. The exosphere, the last stratum reaching about 1000 kilometres above the Earth's surface, is a transitional layer between the atmosphere and the interplanetary space.

1.2 Chemical Composition

The atmosphere is a mixture of various gases that play an important role in the radiation process, the so-called radiatively active gases. Variation in the concentration of such gases affects the energy balances and manifests as the changes

in the thermal and dynamic properties of the atmosphere (Andrews et al., 1987). Our study focuses mainly on greenhouse gases (GHGs) and ozone together with ozone-depleting substances (ODSs). GHGs concentration increase is the principal forcing connected with global climate change and the temperature increase in the troposphere. Ozone strongly influences the stratospheric conditions and its concentration has declined due to the anthropogenic emissions of ODSs (WMO, 2018).

1.2.1   Greenhouse Gases

Radiatively active gases are an essential group of gases in the atmosphere. These gases absorb or emit radiation in some relevant wavelength and therefore influence the radiation budget in the atmosphere. An important term for describing radiation balance is radiative forcing (expressed in Watts per square metre), defined as the net change in downward energy flux at the tropopause after allowing for stratospheric temperatures to readjust to radiative equilibrium, while surface and tropospheric temperatures and state variables are fixed at the unchanged values (Myhre et al., 2013). The most naturally represented radiatively active gases are water vapour, carbon dioxide, ozone, methane, and nitrogen oxides. In addition to natural processes, these gases are also produced as a human activity product, such as the combustion of fossil fuels or land use conversion. The observed increase in the concentration of radiatively active gases is directly connected to the anthropogenic emissions (Masson-Delmotte et al., 2018).

Table 1.1: Constituents of the Earth's dry atmosphere, data valid in 2011 from (Hartmann, 2015). CO_2, CH_4, and N_2O values from the (Dlugokencky and Tans, 2021).

Compound	Fraction by volume
Nitrogen	78.08
Oxygen	20.95
Argon	0.934
Carbon Dioxide (January, 2021)	0.0415
Neon	$18.18 \cdot 10^{-4}$
Helium	$5.24 \cdot 10^{-4}$
Methane (December, 2020)	$1.892 \cdot 10^{-4}$
Krypton	$1.14 \cdot 10^{-4}$
Hydrogen	$0.5 \cdot 10^{-4}$
Nitrous oxide (November, 2020)	$0.336 \cdot 10^{-4}$
Carbon monoxide	$0.12 \cdot 10^{-4}$
Ammonia	$0.1 \cdot 10^{-4}$
Xenon	$0.087 \cdot 10^{-4}$
Water vapour	Variable
Ozone	Variable
Sulphur dioxide	$0.1 \cdot 10^{-6}$
Nitrogen dioxide	$0.001 \cdot 10^{-6}$
Other constituents	Trace amount

Gases that absorb and emit infrared radiation are also referred to as greenhouse gases as they strongly influence the warming of the troposphere. The most common GHGs are carbon dioxide, methane and nitrous oxide (see Tab. 1.1). Atmospheric CO_2 reached 148% of the pre-industrial level in 2019 (WMO, 2020) and an 11% increase since 2000. Carbon dioxide caused about 82% of the increase in radiative forcing over the past decade, being the primary driver of related changes. The mole fraction of methane in 2019 exceeded 260% of the pre-industrial level (WMO, 2020). The mean annual increase of CH_4 dropped almost to zero between 1999-2006 (Fig. 1.3) and has been growing again since 2007. For nitrous oxide was recorded a relatively small increase compared to the pre-industrial value - approximately 27% (WMO, 2020). In addition to CO_2, CH_4 and N_2O, the stratospheric ozone-depleting chlorofluorocarbons (CFCs) are other prominent GHGs. CFCs and most halons decrease as they are regulated. Some hydrochlorofluorocarbons (HCFCs) and hydrofluorocarbons (HFCs) are also potent greenhouse gases increasing at relatively rapid rates although they are still at low levels (WMO, 2020).
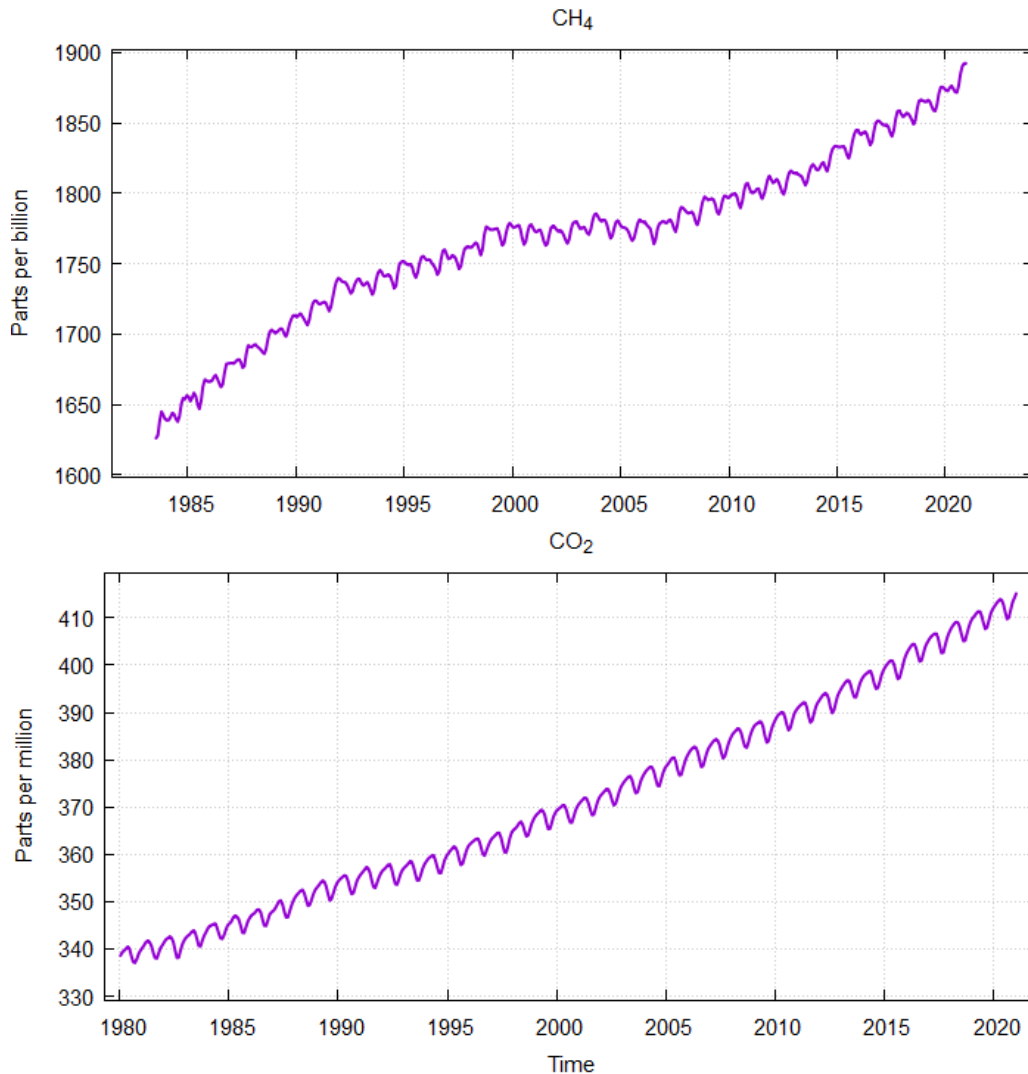

Figure 1.3: Globally averaged marine surface monthly mean concentration for carbon dioxide and methane. Data from (Dlugokencky and Tans, 2021).

Further development of GHGs is essential for future atmospheric evolution. The Representative Concentration Pathway (RCP) scenarios were created for projections of GHGs concentrations (IPCC, 2013). There are initially the four RCPs labelled after a possible range of radiative forcing values in 2100 (relatively to 1750) in W/m² - RCP2.6, RCP4.5, RCP6.0, and RCP8.5. Based on the RCPs, expected changes in global surface temperature and global sea level can be estimated, as shown in Tab. 1.2. Fig. 1.4 then shows the overall evolution of GHGs over the 21st century based on these scenarios.

Table 1.2: Projected changes in global mean surface air temperature and global mean sea level for 2081-2100 relative to 1986–2005, based on the Coupled Model Intercomparison Project Phase 5 (CMIP5) ensemble. Values from (IPCC, 2013).

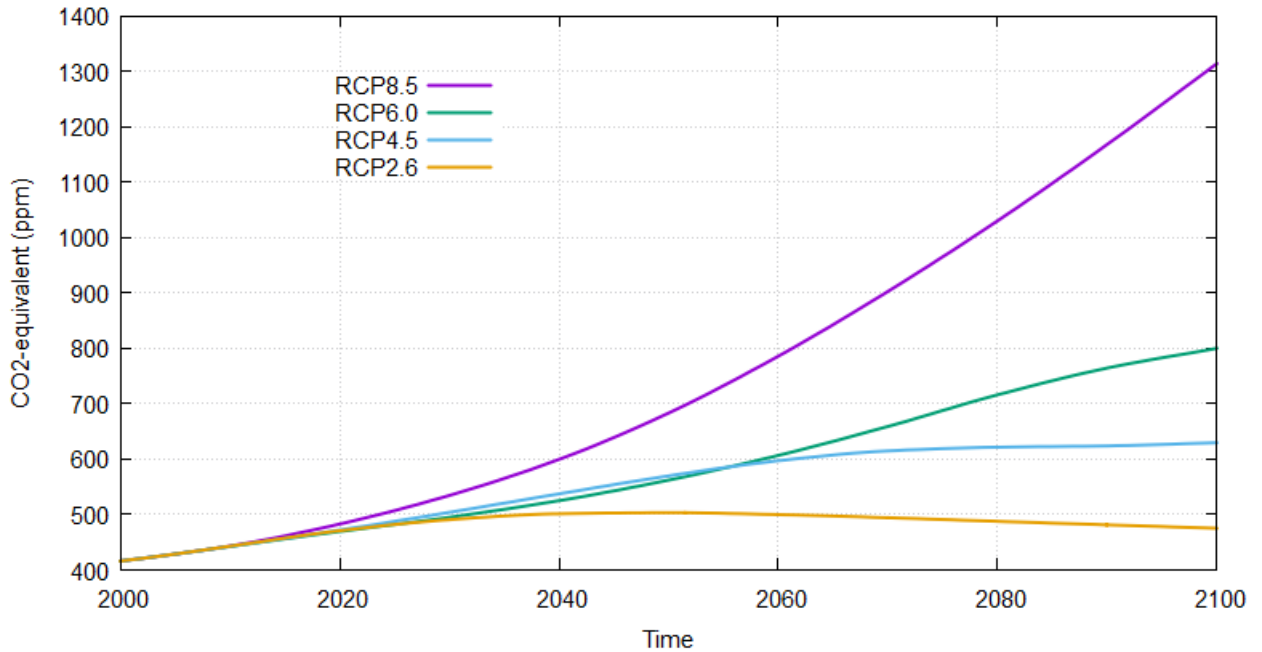| Scenario	Temperature [°C]	Sea level [m]
RCP2.6	0.4 to 1.6	0.17 to 0.32
RCP4.5	0.9 to 2.0	0.19 to 0.33
RCP6.0	0.8 to 1.8	0.18 to 0.32
RCP8.5	1.4 to 2.6	0.22 to 0.38

Figure 1.4: GHGs concentrations in parts per million (ppm) CO2-equivalent according to the four RCPs. Data downloaded from the RCP Database version 2.0 https://tntcat.iiasa.ac.at/RcpDb/dsd?Action=htmlpage&page=about.

1.2.2 Ozone-depleting Substances

Another group of substances in the atmosphere important to our study are ODSs. Those chemical species contribute to the destruction of the ozone layer

and include two main groups, i.e. CFCs and HCFCs. ODSs have relatively long lifetimes in the troposphere (in order of years), where there are produced. However, they are transported into the stratosphere by turbulent mixing (exchange resulted by the turbulent fluctuation of parameters such as velocity and temperature), where they catalyse the breakdown of ozone.

In the 1980s, reductions of up to 70% in the ozone column were observed during spring over Antarctica (Farman et al., 1985). This decrease was naturally associated with higher concentrations of ODSs in the atmosphere caused by the high production of these substances by humans. The Montreal Protocol, signed in 1987 with effect from 1989, obliged the signatory countries to a significant reduction in ODSs production. This and other international agreements led to a decrease in the atmospheric burden of ODSs, as shown in Figure 1.5.

Due to the reduction of ODSs, the first signs of recovery of the Antarctic ozone hole was observed. Scientific Assessment of Ozone Depletion: 2018 (WMO, 2018) describes the future development of ozone based on chemistry-climate models' projections (considering RCP6.0 for GHGs). The Antarctic ozone hole expected to gradually close, with the total ozone column in spring returning to 1980 values about 2060. Around 2030, ozone recovery is expected in the Arctic and Northern hemisphere (NH) mid-latitude region. Southern hemisphere (SH), mid-latitude ozone is expected to return around mid-century.
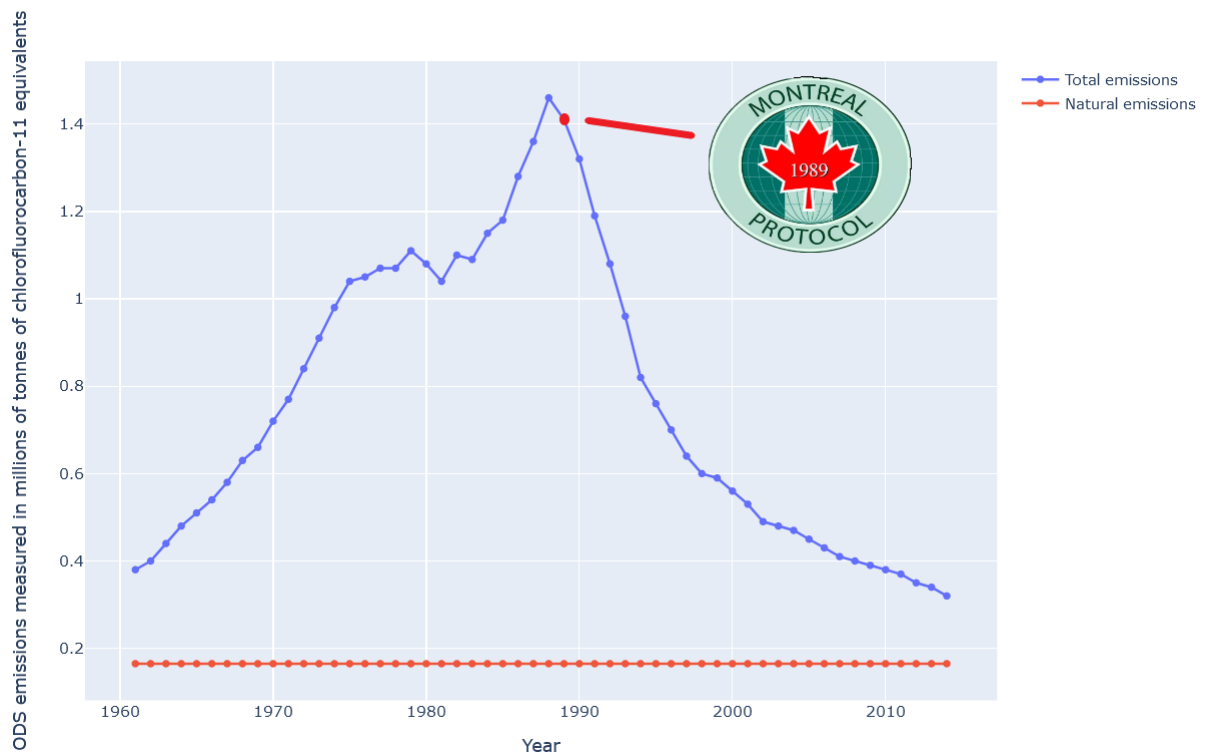

Figure 1.5: Global emissions of ODSs from 1960 to 2014. Emissions of ODSs are weighted by their potential to destroy ozone (their ozone-depleting potential). Total emissions include emissions from natural and man-made sources. Data from (Hegglin et al., 2014).

CO_2, CH_4 and N_2O, as they affect chemical cycles and the stratospheric circu-

lation, will be the main factors for the evolution of ozone in the second half of the 21st century outside Antarctica (WMO, 2018). Stronger climate forcing results in an increase in ozone redistribution. By 2100, even higher concentrations of stratospheric ozone in the Arctic and mid-latitudes compared to 1960–1980 average values are expected. In the Arctic during springtime, the increase is expected about 35 Dobson units (DU) for RCP4.5 and 50 DU for RCP8.5. In the tropics, a decrease is expected by approximately 5 DU for RCP4.5 and 10 DU for RCP8.5 (WMO, 2018).

Chapter 2

Middle Atmospheric Climatology and Transport

The middle atmosphere is a region from the tropopause to the homopause (about 10–110 km) and including the stratosphere, mesosphere, and lower thermosphere (Andrews et al., 1987). Circulation in the middle atmosphere affects the transport of chemical species and heat redistribution, and may strongly affect tropospheric condition too.

2.1 Climatology of the Middle Atmosphere

To illustrate average conditions and seasonal variability in the middle atmosphere, we have analysed data from the chemistry-climate model EMAC-L90MA (Jöckel et al., 2010, 2016), included in phase 1 of the Chemistry–Climate Model Initiative (CCMI-1) (Morgenstern et al., 2017). We have calculated vertical profiles of the zonal averages for the 1960-2000 period for the temperature series and the zonal velocities.

2.1.1 Temperature

Fig. 2.1 illustrates the seasonal variation of the temperature between 100 hPa and 0.001 hPa (roughly delimiting the middle atmosphere). We may see clear stratification with maximum temperatures around the stratopause region and minima connected to the tropopause and mesopause regions. Absolute temperature minimum is found at the summer mesopause and absolute maximum at summer stratopause. Both the stratopause and mesopause are clearly elevated over the polar regions in winter and to some degree also in autumn.
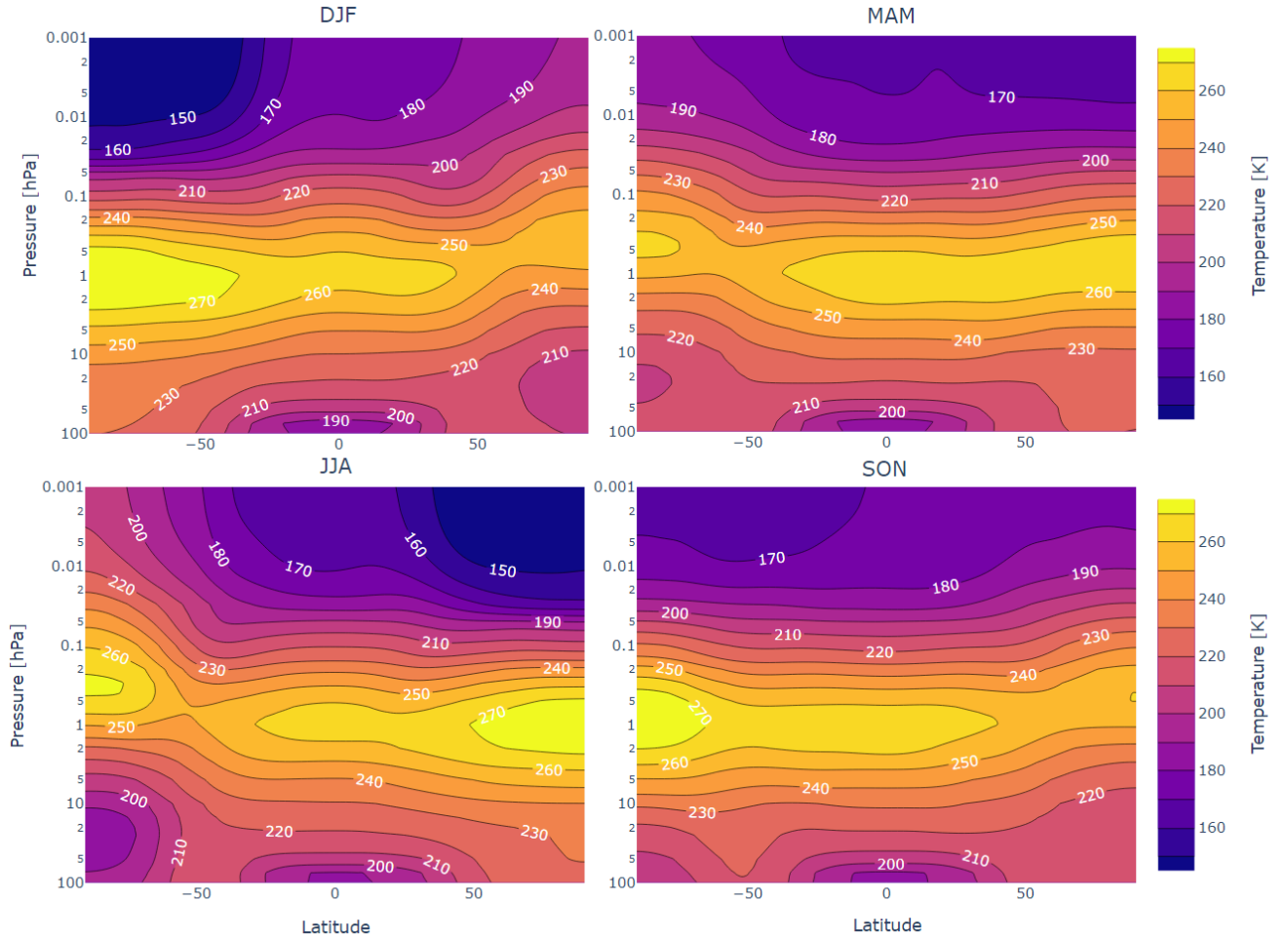
Figure 2.1: Seasonal averages of the zonal means of temperature from the chemistry-climate model EMAC-L90MA REF-C2 scenario for 1960-2000.

2.1.2 Zonal Winds

Seasonal variations of the zonal winds are shown in Fig. 2.2. There is a clear distinction between the summer and winter zonal circulation in the middle atmosphere. The winter hemisphere is connected to the westerlies and the summer to the easterlies. Stronger winds are generally found in the SH. There is also a hemispheric difference in spring. The transition from the winter to the summer circulation is slower in the SH, where we may still see relatively strong westerlies during spring. The winter circulation is formed already in autumn and during winter, there is a very distinct stratospheric polar region with the strongest winds within the middle atmosphere. This circulation is called the polar night jet or the polar vortex.
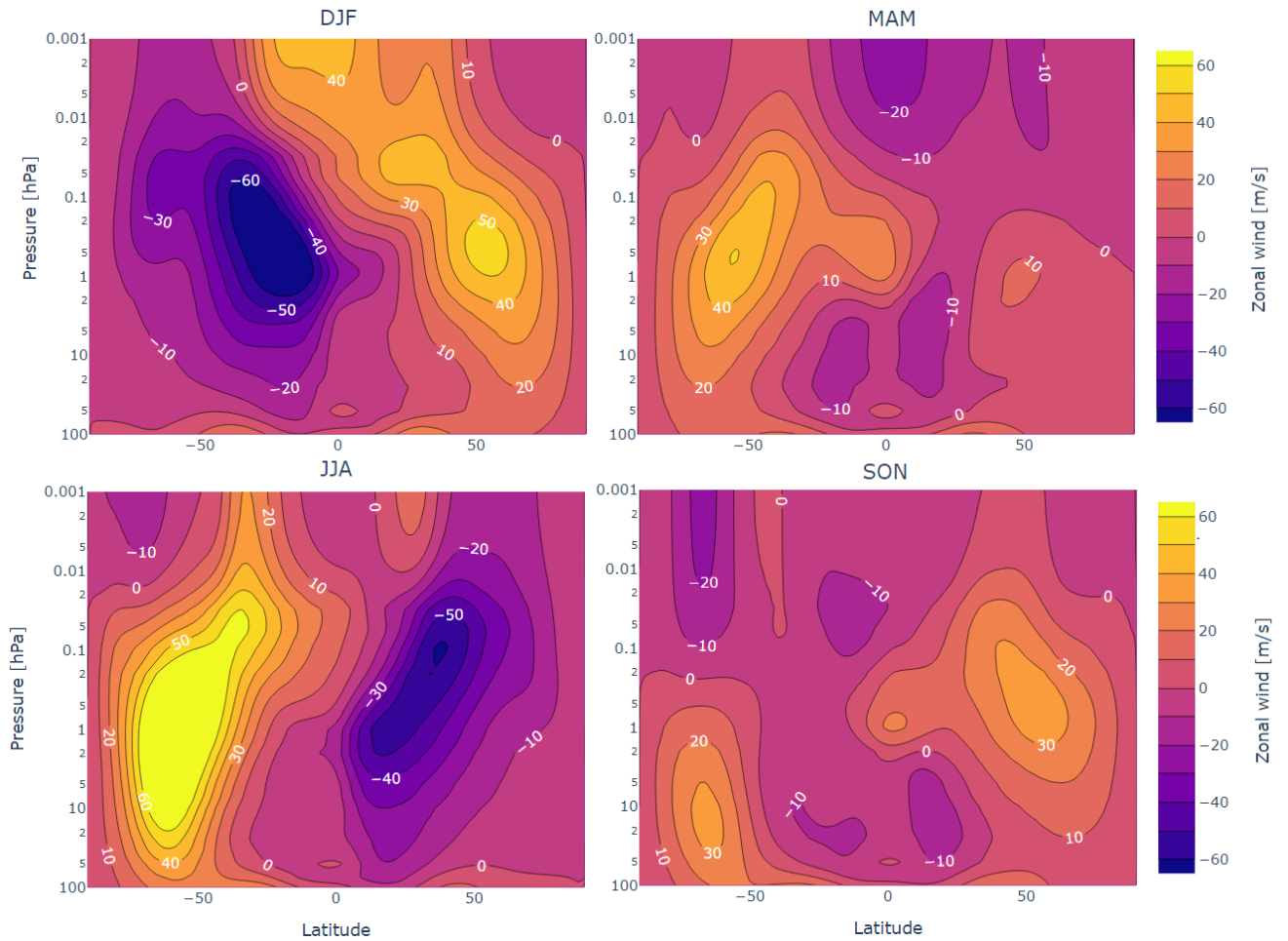
Figure 2.2: Seasonal averages of the zonal means of zonal winds from the chemistry-climate model EMAC-L90MA REF-C2 scenario for 1960-2000.

2.2 Polar Vortex

During the polar night, a strong closed westerly circulation forms in the upper troposphere and stratosphere around the poles because of the high latitudinal temperature gradient that grows due to the negative radiation balance in the polar regions (see Fig. 2.3). The polar vortex isolates the cold polar air from the rest of the stratospheric air, making it even colder. Polar vortices are not equally strong and stable in both hemispheres. The northern polar vortex is weaker and less stable. That is because it is under the stronger influence of the Rossby planetary waves that result from the orography related disturbances like the temperature gradients that are pronounced between land and ocean (Mohanakumar, 2008). As the NH is covered by more land than in the south, these waves are more significant in the Arctic. A weaker polar vortex leads to higher temperatures and also to greater air exchange with the mid-latitudes. Both these factors contribute to the fact that ozone depletion is much less significant in the Arctic than in Antarctica.

The polar jet stream is connected to the polar vortex's outer boundary. In the troposphere, it is a variable flow that strongly influences weather pattern. It

also provides an important coupling mechanism for the middle atmosphere and the troposphere, because the disturbances in the polar vortex may be manifested in the polar jet stream that influences the tropospheric conditions too.
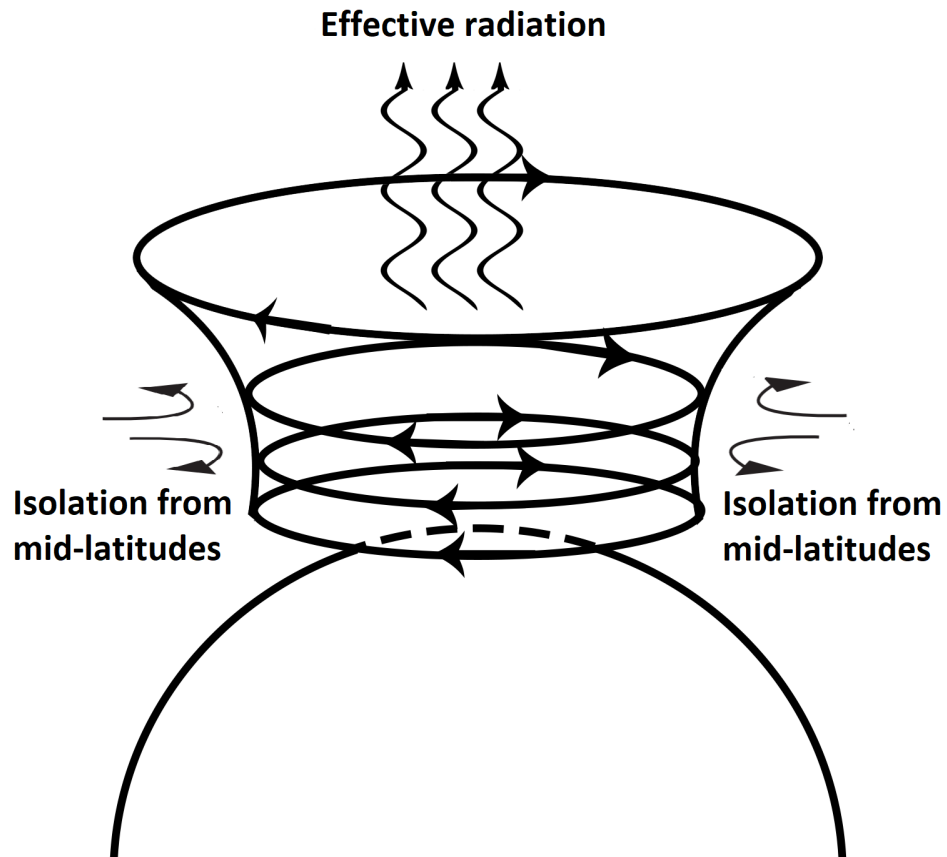
Effective radiation

Isolation from mid-latitudes

Isolation from mid-latitudes

Figure 2.3: Scheme of the polar vortex

2.3 Brewer-Dobson Circulation

The Brewer-Dobson circulation (BDC) describes a wide range of meridional and vertical, especially stratospheric and mesospheric, motions explaining the uneven distribution of ozone in the atmosphere. Originally, analysis of these movements was inspired by the measurements of the British physicist and meteorologist G. M. B. Dobson. Using an ozone spectrometer, he found that most ozone is not located in the tropical areas where it is produced but in high latitudes. Moreover, the Canadian and English physicist A. W. Brewer analysed distribution of the water vapour concentration observed in the late 1940s and found that the stratosphere is almost dry. That led to an idea that there had to be a transport of the tropospheric air into the stratosphere in the tropics and related transport of the ozone from tropics to high latitudes.

2.3.1 Basic Description

The transfer of ozone is realized by the slow rise of tropical air from the tropopause to the stratosphere, where it heads towards the pole. Flow is upward in the tropics, extends into the middle and upper stratosphere, and downward in middle and high latitudes.

The BDC consists of two parts based on a different mechanism. The first is a slow residual circulation driven by planetary waves. The second part is a fast isentropic mixing (Butchart, 2014). The BDC is more robust in the winter hemisphere and practically does not exist in the summer hemisphere. The difference is linked mainly to the deep branch of the BDC (Birner and Bönisch, 2011), which forms the central part of the residual mean circulation in the winter middle and upper stratosphere. Besides the central part, there are also faster shallow branches in the subtropical lower stratosphere of both hemispheres. Those exist throughout the year, and hence, the pronounced seasonality in the upwelling and downwelling motions is connected to the deep branch. The BDC is schematically illustrated in Fig. 2.4.
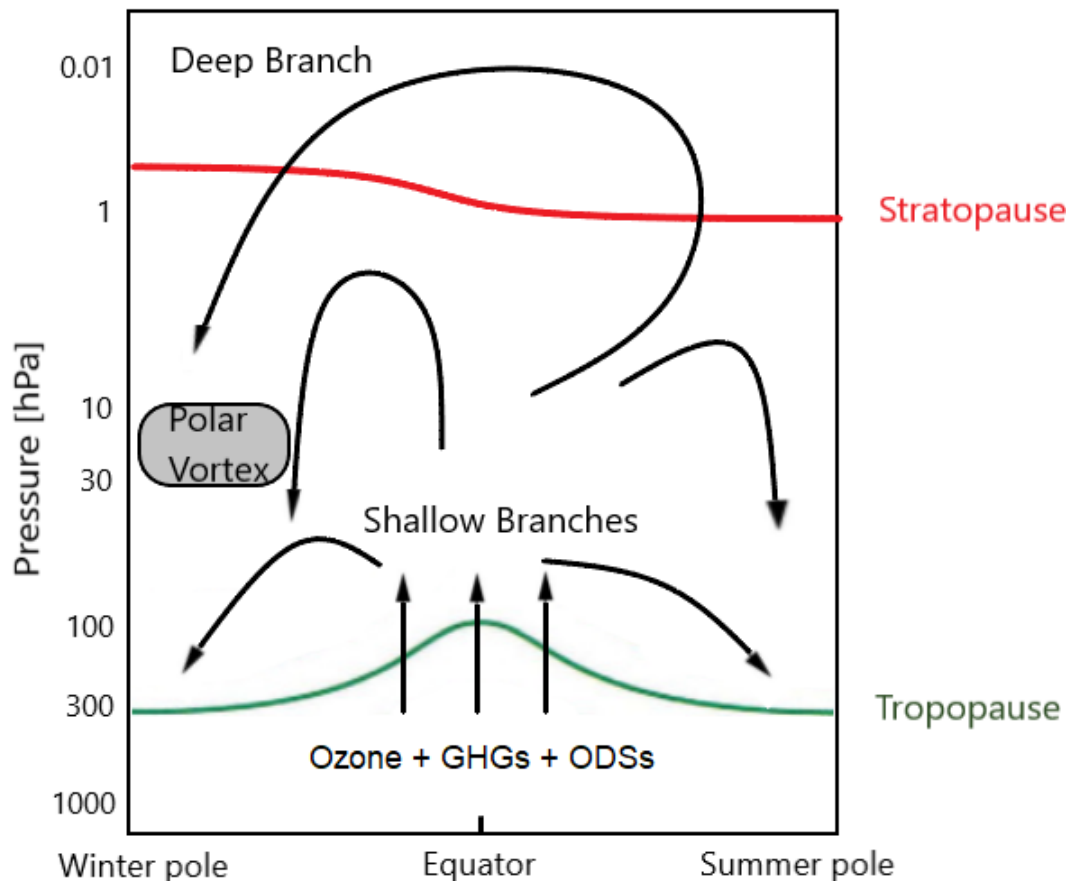

Figure 2.4: Scheme of the Brewer-Dobson circulation

2.3.2 Models Describing the Brewer-Dobson Circulation

Since the BDC is closely related to mass transfer, it is advantageous to use the zonally averaged mass circulation for the description. Mass circulation is defined as the transport of long-lived trace elements that are largely nonreactive and have

very long lifetimes. Thus, their distribution in the stratosphere is given primarily by air circulation.

The BDC is frequently quantified by residual-mean circulation described by the vertical $\overline{w}^*$ and meridional $\overline{v}^*$ residual velocity in the transformed Eulerian mean (TEM). The TEM is based on the Eulerian mean equations supplemented by eddy terms combining eddy and mean transport contributions into a single quantity. Velocities in the TEM in log-pressure coordinates are defined by (Andrews et al., 1987):

$$\overline{v}^* = \overline{v} - \frac{1}{\rho_0}\left(\frac{\rho_0\overline{v'\theta'}}{\overline{\theta_z'}}\right)_z = -\frac{1}{\rho_0\cos\phi}\psi_z^*, \tag{2.1}$$

$$\overline{w}^* = \overline{w} + \frac{1}{a\cos\phi}\left(\frac{\cos\phi\,\overline{v'\theta'}}{\overline{\theta_z'}}\right)_\phi = \frac{1}{a\rho_0\cos\phi}\psi_\phi^*. \tag{2.2}$$

where an overbar describes zonal mean, $()_x$ represents partial derivative with respect to x, v/w is the northward/vertical velocity, ϕ is latitude, θ is potential temperature, z is log-pressure height, a is the radius of the Earth, $\rho_0 = \exp(z/H)$ where H is the density scale height taken as 6800 m in the log-pressure coordinates, and ψ^* is the residual stream function.

From Eq. 2.1 and 2.2 follow that the flow velocity components can be calculated as derivatives of the scalar residual stream function $\psi^*(z,\phi)$. Thus, knowledge of this scalar function provides complete information about the flow. The stream function has a clear geometric meaning. Curves with a constant value of the stream function are called streamlines, which are tangent to the flow velocity vector.

2.3.3 Mechanism of the Brewer-Dobson Circulation

The BDC is driven mainly by atmospheric waves called Rossby waves (RW). The dominant planetary-scale RW always propagate westward with respect to the background flow (Butchart, 2014). RW transport air vertically and westward from the tropopause. Sucked up air in the tropics descents in the middle and high latitudes, which results from the law of conservation of angular momentum. However, a reverse pole-to-equator flow would have to exist at higher levels to balance the angular momentum budget, which is not observed (Butchart, 2014).

In the mesosphere, the mass transport is from the summer to the winter pole. This part of the circulation is driven primarily by upward propagating inertia-gravity waves. Inertia-gravity waves can propagate through both mean easterlies and westerlies, unlike RW, and their impacts on the mean zonal flow can be positive or negative, depending on their phase velocities (Plumb, 2002).

Although planetary waves forcing explain the majority of both parts of the BDC circulation, the are also other air movements, especially in the tropics, that cannot be explained by the wave drag. One example is the observed maximum in the tropical upwelling on the summer side of the equator, which remains poorly understood (Butchart, 2014).

Chapter 3

Data and Methods

Climate models are used to analyse climatic elements, their changes and predict future atmospheric developments. Climate models use quantitative methods to simulate the major climate drivers' interactions, including the atmosphere, oceans, land surface, and ice.

3.1 Chemistry–Climate Model Initiative

Results of this thesis are based on data from climate models that are used within the CCMI-1 (Morgenstern et al., 2017). The CCMI-1 is a united activity of the International Global Atmospheric Chemistry (IGAC) and Stratosphere–troposphere Processes And their Role in Climate (SPARC) projects, combining physical climate models with a representation of atmospheric chemistry. The CCMI-1 is based on previous chemistry-climate models such as the Chemistry–Climate Model Validation (CCM-Val) and the Atmospheric Chemistry and Climate Model Intercomparison Project (ACCMIP) (Morgenstern et al., 2017). The CCMI-1 contains 20 models, but only some were used in this thesis (Table 3.1).

Table 3.1: List of used models from the CCMI-1. Models marked with an asterisk were subsequently excluded from the analysis based on outliers (Figure 3.1).

Model name	References
CMAM	(Jonsson et al., 2004; Scinocca et al., 2008)
ACCESS-CCM	(Morgenstern et al., 2009, 2013)
GEOSCCM	(Molod et al., 2012, 2015; Oman et al., 2011, 2013)
MRI-ESM1r1	(Deushi and Shibata, 2011; Yukimoto et al., 2012)
SOCOL3	(Revell et al., 2015; Stenke et al., 2013)
EMAC-L90MA	(Jöckel et al., 2010, 2016)
CCSRNIES-MIROC3.2	(Imai et al., 2013; Akiyoshi et al., 2016)
CESM1-WACCM	(Garcia et al., 2017; Marsh et al., 2013; Solomon et al., 2015)
ULAQ-CCM*	(Pitari et al., 2016; Visioni et al., 2018)
NIWA-UKCA*	(Stone et al., 2016)

The CCMI-1 models individually differ in their horizontal resolution and vertical grid. However, we have prepocessed all the series and interpolated the data into a common grid of 91 latitudes and 19 pressure levels between 100 hPa and 0.1 hPa (100, 90, 80, 70, 50, 30, 20, 15, 10, 7, 5, 3, 2, 1.5, 1, 0.5, 0.3, 0.2 and 0.1 hPa).

3.1.1 CCMI-1 Experiments

There is a number of model experiments conducted for the CCMI-1. The primary simulation analysed in this thesis is REF-C2. REF-C2 is a set of simulations covering the period 1960–2100. REF-C2 follow the IPCC Special Report on Emissions Scenarios (SRES) A1 scenario (WMO, 2011) for ODSs and the RCP6.0 for GHGs, tropospheric ozone precursors, and aerosol and aerosol precursor emissions (Meinshausen et al., 2011). Furthermore, two variants of the REF-C2 experiment were studied. The SEN-C2-fODS and SEN-C2-fGHG scenarios allow a comparison of the influence of ODSs and GHGs, as ODSs and GHGs are fixed at their 1960 levels in the SEN-C2-fODS and SEN-C2-fGHG scenarios respectively (Morgenstern et al., 2017).

All models mentioned in Table 3.1 provide data for the REF-C2 experiment. Data available for the SEN-C2-fGHG simulation were from CCSRNIES-MIROC3.2, ACCESS-CCM, EMAC-L90MA, and CMAM models and from the same models without EMAC-L90MA for the SEN-C2-fODS experiment.

3.2 Residual Stream Function

Analysis of transport between the stratosphere and mesosphere was based on the annual and seasonal averages of the residual stream function ψ^* provided by the authors of the study (Eichinger and Šácha, 2020). Standard seasons were considered - December-February (DJF), March-May (MAM), June-September (JJA) and September-November (SON). An example of the stream function for DJF is illustrated in Fig. 3.1. Two distinct outliers are clearly seen there, i.e. NIWA-UKCA and ULAQ-CCM. Those were not considered for further analysis.

The vertical mass flux F between two parallels can be expressed at a constant pressure level p_0 as (Eichinger and Šácha, 2020):

$$F = 2\pi a^2 \rho_0 \int_{\phi_1}^{\phi_2} \overline{w}^* \cos \phi \, \mathrm{d}\phi. \tag{3.1}$$

From the combination of Eq. 2.2 and 3.1 follows:

$$F = 2\pi a \int_{\phi_1}^{\phi_2} \psi_\phi^*(p_0, \phi) \, \mathrm{d}\phi = 2\pi a [\psi_\phi^*(p_0, \phi_2) - \psi_\phi^*(p_0, \phi_1)]. \tag{3.2}$$

Thus, it is clear that the upward and downward mass flow at a given pressure level can be obtained simply from the residual stream function's values. However, the stratopause is not at one pressure level, and it is not possible to use this method. Instead, a procedure based on derivatives of the residual stream function (the first part of Eq. 3.2) was used.

The numerical latitudinal derivatives of the residual stream function at the available pressure levels were computed from the equation below:

$$\psi_\phi^*(\phi_i, p_0) = \frac{\psi^*(\phi_{i+1}, p_0) - \psi^*(\phi_i, p_0)}{\phi_{i+1} - \phi_i}. \tag{3.3}$$

Multiplied by the parameter $2\pi a$, these derivatives represent the vertical mass flow for a given latitude and pressure. The value of the mass flux through the stratopause can be obtained by linear interpolation as:

$$\psi_\phi^*(\phi_0, p_s) = \psi_\phi^*(\phi_0, p_1) + (p_s - p_1)\frac{\psi_\phi^*(\phi_0, p_2) - \psi_\phi^*(\phi_0, p_1)}{p_2 - p_1}, \tag{3.4}$$

where p_s is the stratopause pressure corresponding to the latitude ϕ_0, and p_1, p_2 are the nearest lower and higher pressures from the vertical grid.
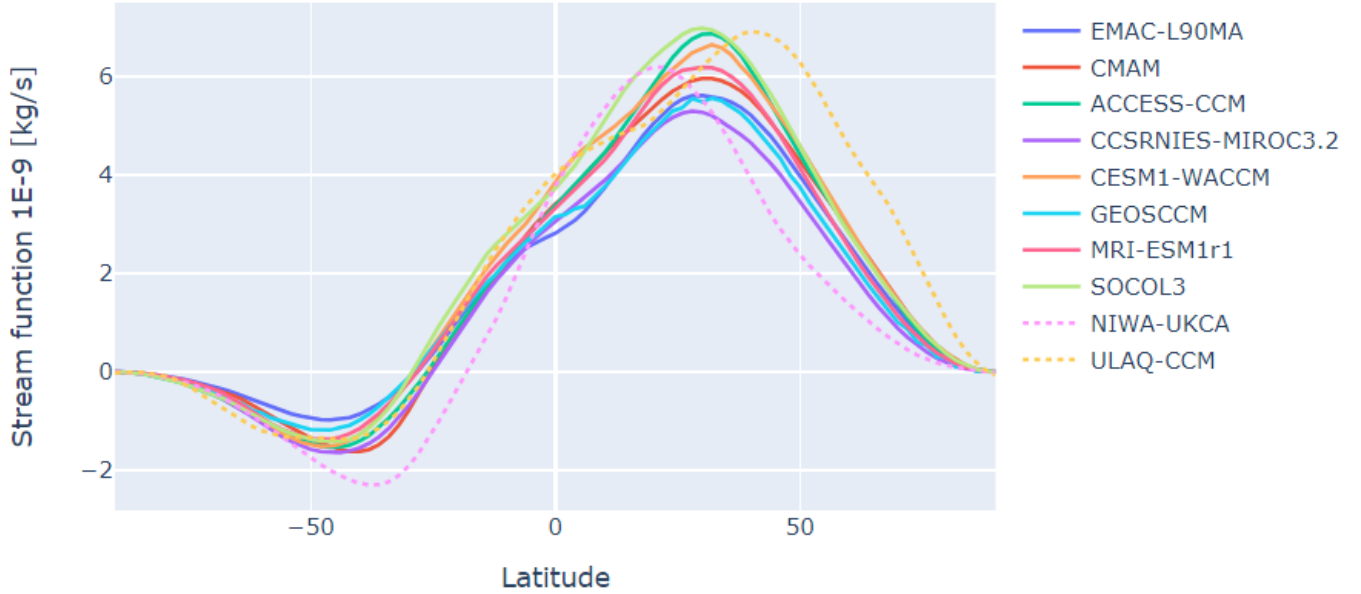
Figure 3.1: Residual stream function zonal mean for DFJ at 50 hPa from REF-C2, 1960-2080. Multiplied by $2\pi a$. Values from NIWA-UKCA and ULAQ-CCM differ significantly from other models.

3.3 Trends

Trends of the studied variables are important for the quantitative assessment of future development. The trends in this work were computed using linear regression based on the least squares method. To assess the reliability of the trends, a two-sided p-value was computed for a hypothesis test whose null hypothesis is that the slope is zero, using the Wald test with t-distribution of the test statistic. If a p-value is less than 0.05, the null hypothesis is rejected, and we consider the linear trend to be statistically significant at level 0.95.

Chapter 4

Results

The following chapter introduces the residual stream function analysis results based on the CCMI-1 models' data. First, to understand the initial state of vertical movements in the stratosphere and lower mesosphere, the climatology of the residual stream function and vertical distribution of mass flux is presented for 1960-2000 for the REF-C2 scenario. Next, the transport itself through the stratopause is demonstrated. The spatial distribution of mass flux, total downwelling and upwelling motions and their sum were investigated. The difference between hemispheres was also examined based on the analysis of descending movements. All results presented in this chapter are averages from all available models.

4.1   Residual Stream Function and Vertical Mass Flux Climatology

Fig. 4.1 and 4.2 show seasonal changes in vertical transport in the stratosphere and lower mesosphere. Fig. 4.1 presents the seasonal averages of the residual stream function, illustrating changes in the circulation cells on the NH and SH. Fig 4.2 shows the vertical mass flux connected to the upwelling and downwelling. The strong upwelling is evident for all seasons in the tropics in the lower and middle stratosphere. Seasonality in upwelling is not that strong as for downwelling. There are noticeable differences in the intensity of descending movements between the winter and summer hemispheres. Downwelling in the NH for DJF (Fig. 4.2a) is more powerful than for JJA in the SH (Fig. 4.2c). For DJF, the upward movements are the strongest, and there is also a relatively perceptible shift in upwelling towards the summer pole. The shift is also clearly visible in the seasonal variation of the residual stream function in Fig. 4.1. For other seasons, most of the changes are apparent mainly at higher altitudes. For the higher stratosphere, we see a decline in tropical upwelling. Except for SON (Fig. 4.2d), the air even starts to descend in the tropics in the lower mesosphere. It is most significant again for DJF.
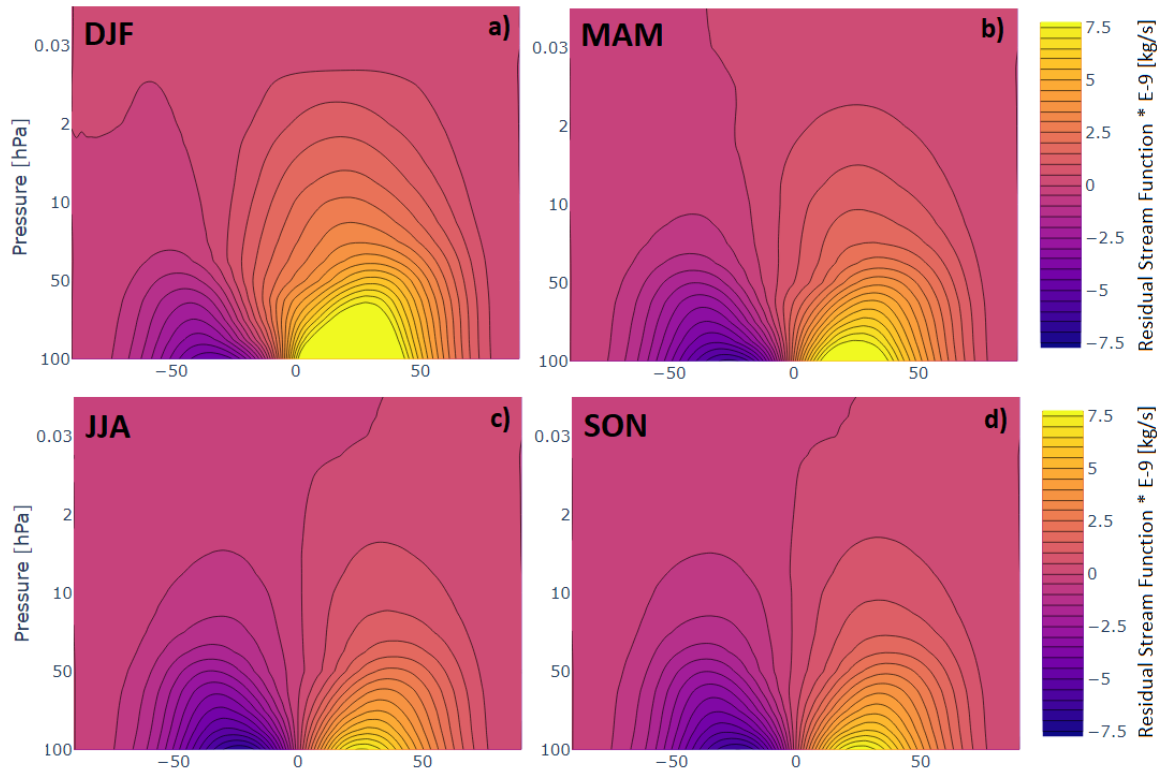
Figure 4.1: Seasonal mean residual stream function climatology for 1960-2000 from the REF-C2 scenario. Multiplied by $2\pi a$.
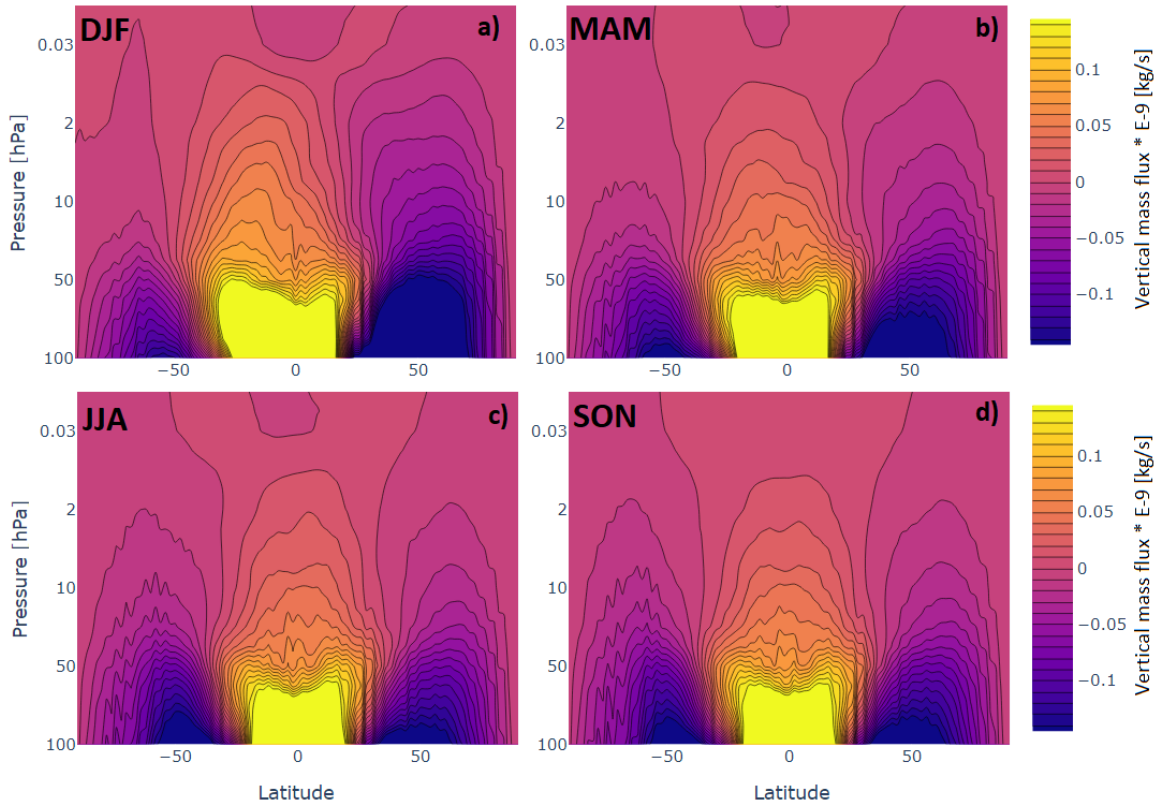
Figure 4.2: Seasonal mean vertical mass flux climatology for 1960-2000 from the REF-C2 scenario. Positive values denote upward motions.

4.2   Transport Between the Stratosphere and Mesosphere

Transport between the stratosphere and mesosphere was calculated by interpolation of vertical mass flux to the height of the stratopause (Eq. 3.4). The stratopause height was calculated as a height of the temperature maximum between 40 and 65 km altitude corresponding to the maximum radiation absorption.

4.2.1   Spatial Distribution

The spatial distribution of vertical mass flux at the stratopause in Fig. 4.3 compares the first and last 30 years of the 1960-2080 period and shows significant inter-seasonal changes as expected. Ascending movements are found in the summer hemisphere and descending movements in the winter hemisphere. The most significant transport is evident for DJF (Fig. 4.3d-f) and JJA (Fig. 4.3j-l), where the deep branch of the BDC is the most pronounced. For MAM (Fig. 4.3g-i) and SON (Fig. 4.3m-o), downwelling can be found on both hemispheres. Comparison of 1960-1990 and 2050-2080 suggests the increase in tropical upwelling for the REF-C2 and SEN-C2-ODS scenarios, visible mainly for DFJ, JJA and the annual average (Fig. 4.3b,d,e,j,k).
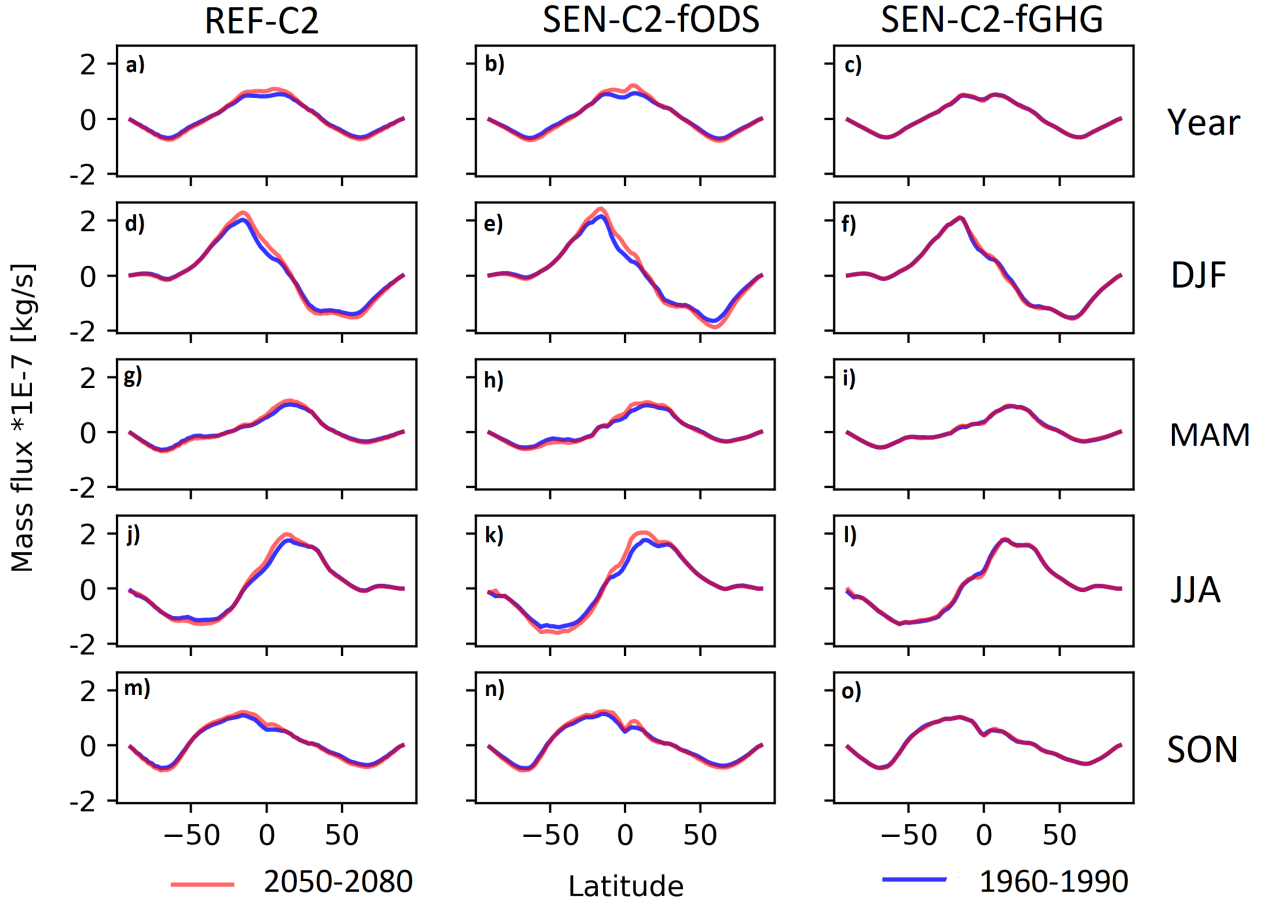
Figure 4.3: Comparison of the spatial distribution of transport through the stratopause for the period 1960-1990 and 2050-2080.

4.2.2 Upward and Downward Motions

Fig. 4.4 shows upward motions summarised across the stratopause over 1960-2000 and 2000-2080. The most intensive upwelling is for summer and winter with average values around $4 \cdot 10^8$ kg/s. For MAM and SON, the values are about half, with SON being slightly stronger than MAM. The expected increases are confirmed for REF-C2 and SEN-C2-fODS, where the growth in upwelling is evident, especially between 2000 and 2080. For SEN-C2-fGHG, the only slight increase in upward movements was detected for JJA and DJF 2000-2080.

Summer and winter also have the greatest values for downwelling, as Fig. 4.5 shows. However, at first glance, it is clear that the downward movements are not as strong as the upward movements, especially for JJA. The same goes for spring and autumn. Reinforcement was also found for descending movements, again only for the REF-C2 and SEN-C2-fODS scenarios.
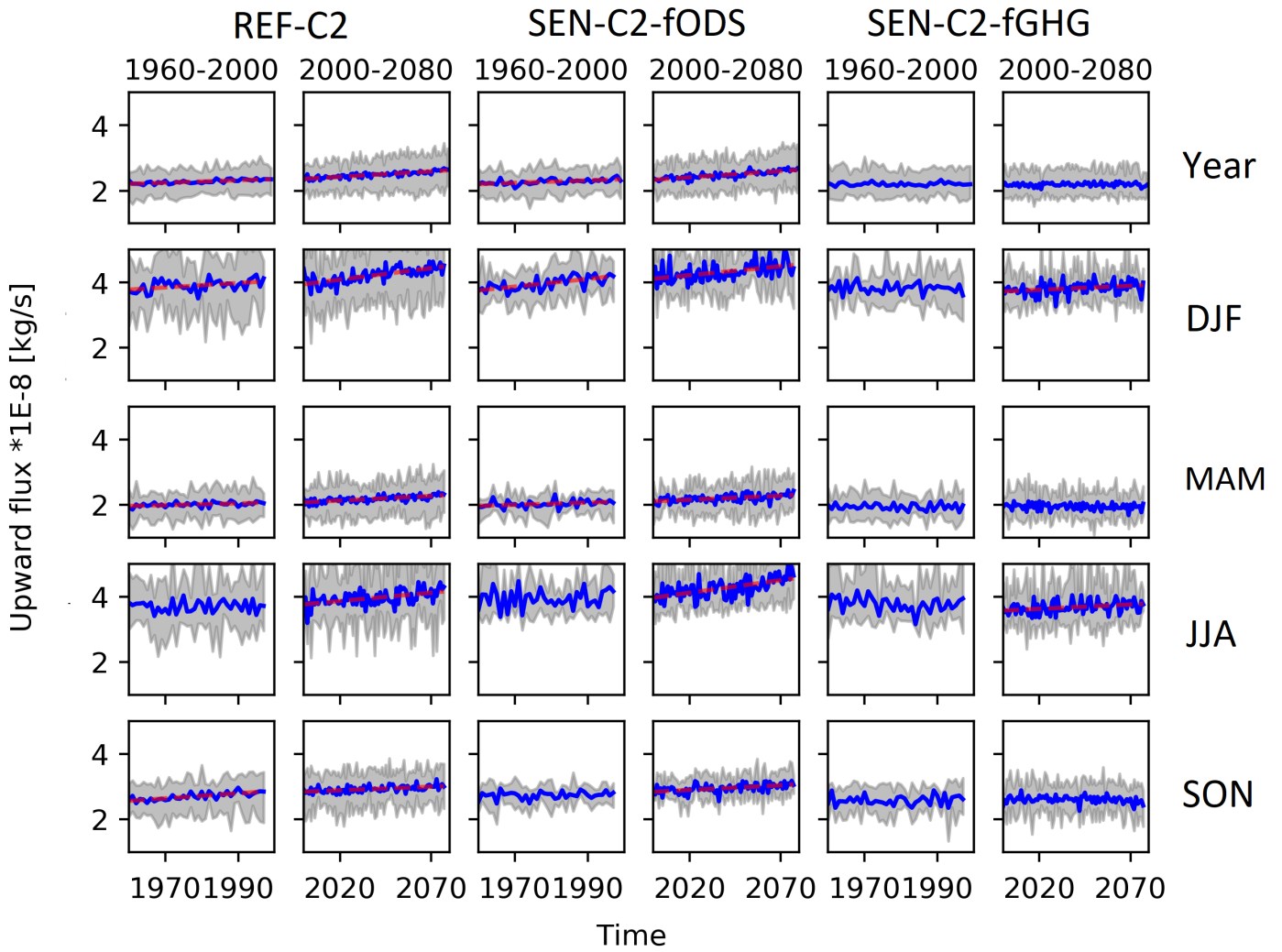
Figure 4.4: Upward motions through the stratopause time lines for 1960-2000 and 2000-2080. A blue line represents the average of models, a gray area is an inter-model scatter. If the statistical significance of a trend for a given period is greater than 0.95, a red line representing that trend is drawn.
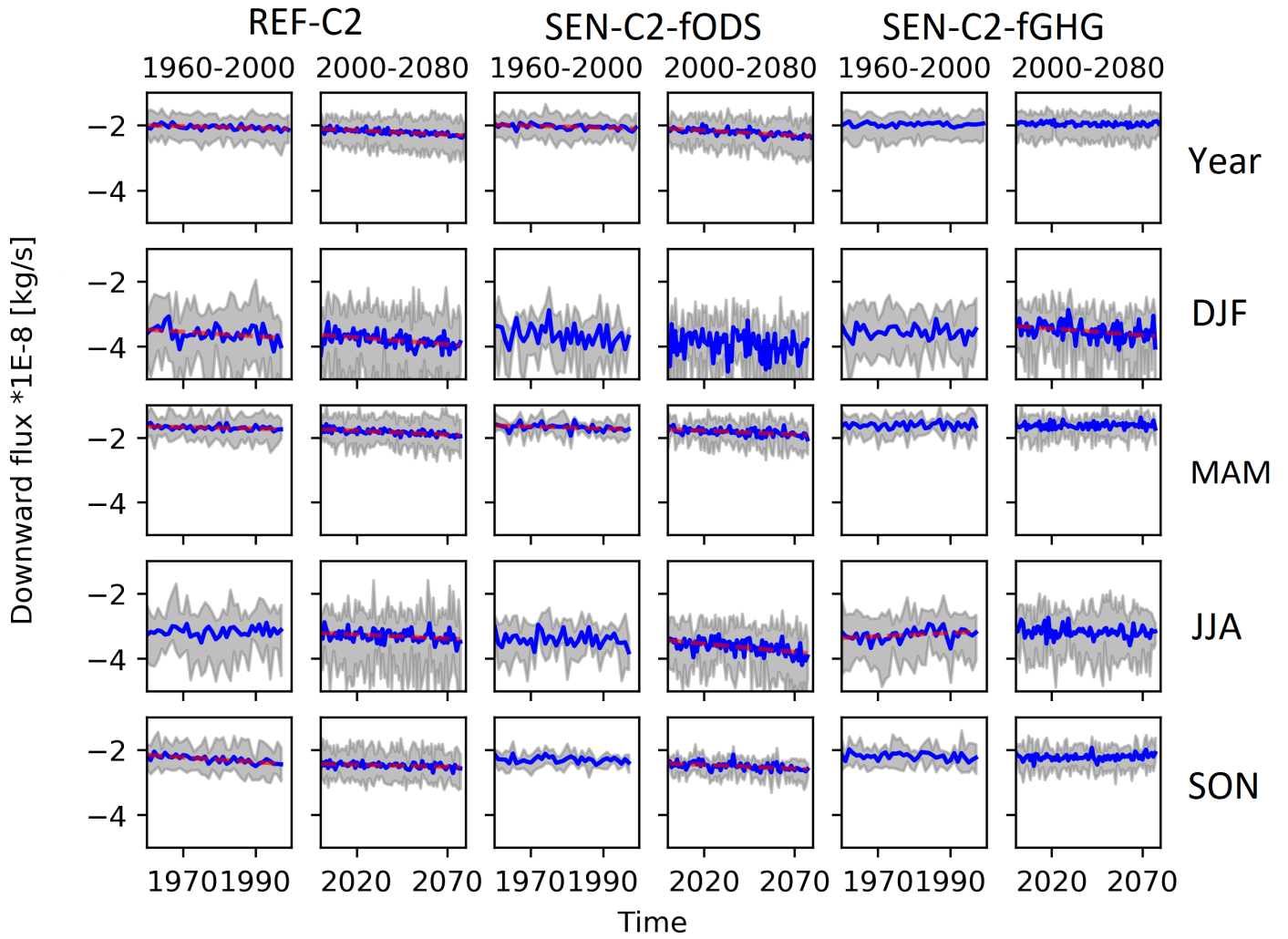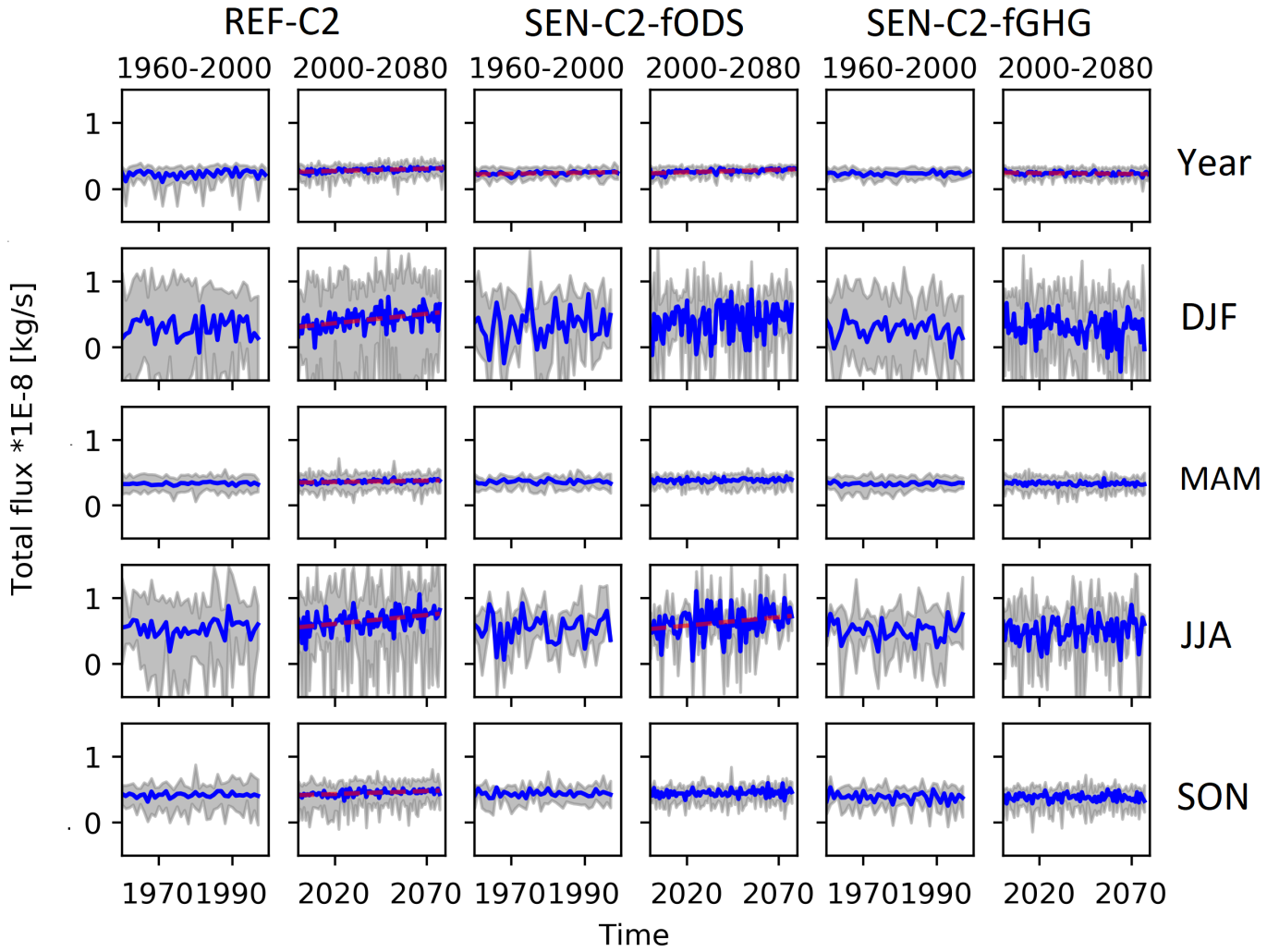
Figure 4.5: Downward motions through the stratopause time lines. A blue line represents the average of models, a gray area is an inter-model scatter. If the statistical significance of a trend for a given period is greater than 0.95, a red line representing that trend is drawn.

Stronger ascending movements over descending ones on average for all seasons are confirmed in Fig. 4.6, showing the total mass flux through the stratopause. The highest values of transport can be found during summer and winter. Future changes in the total flow are not as unambiguous as in upwelling and downwelling separately. However, even here, we see interesting increases for some seasons. For REF-C2 and SEN-C2-fODS, the flow from the stratosphere to the mesosphere increases particularly for DJF and JJA 2000-2020. Considering the GHGs-fixed scenario, changes are not observed.

Figure 4.6: Total mass flux through the stratopause time lines. A blue line represents the average of models, a gray area is an inter-model scatter. If the statistical significance of a trend for a given period is greater than 0.95, a red line representing that trend is drawn.

4.2.3 Hemispheric Differences

Based on the difference between hemispheric descending movements, inter-hemispheric diversity was investigated. Since the downward motions in the individual hemispheres differ fundamentally between the seasons, it is advisable to take JJA with DJF and MAM with SON together for a good comparison, as Fig. 4.7 shows. The most pronounced asymmetry was detected for MOM and SON, where the SH emerged slightly stronger. There is a significant inter-model variance for the annual mean and JJA together with DJF. However, on average, it cannot be said that one hemisphere is stronger than the other. In addition, there is no emerging shift in hemispheric differences in the future.
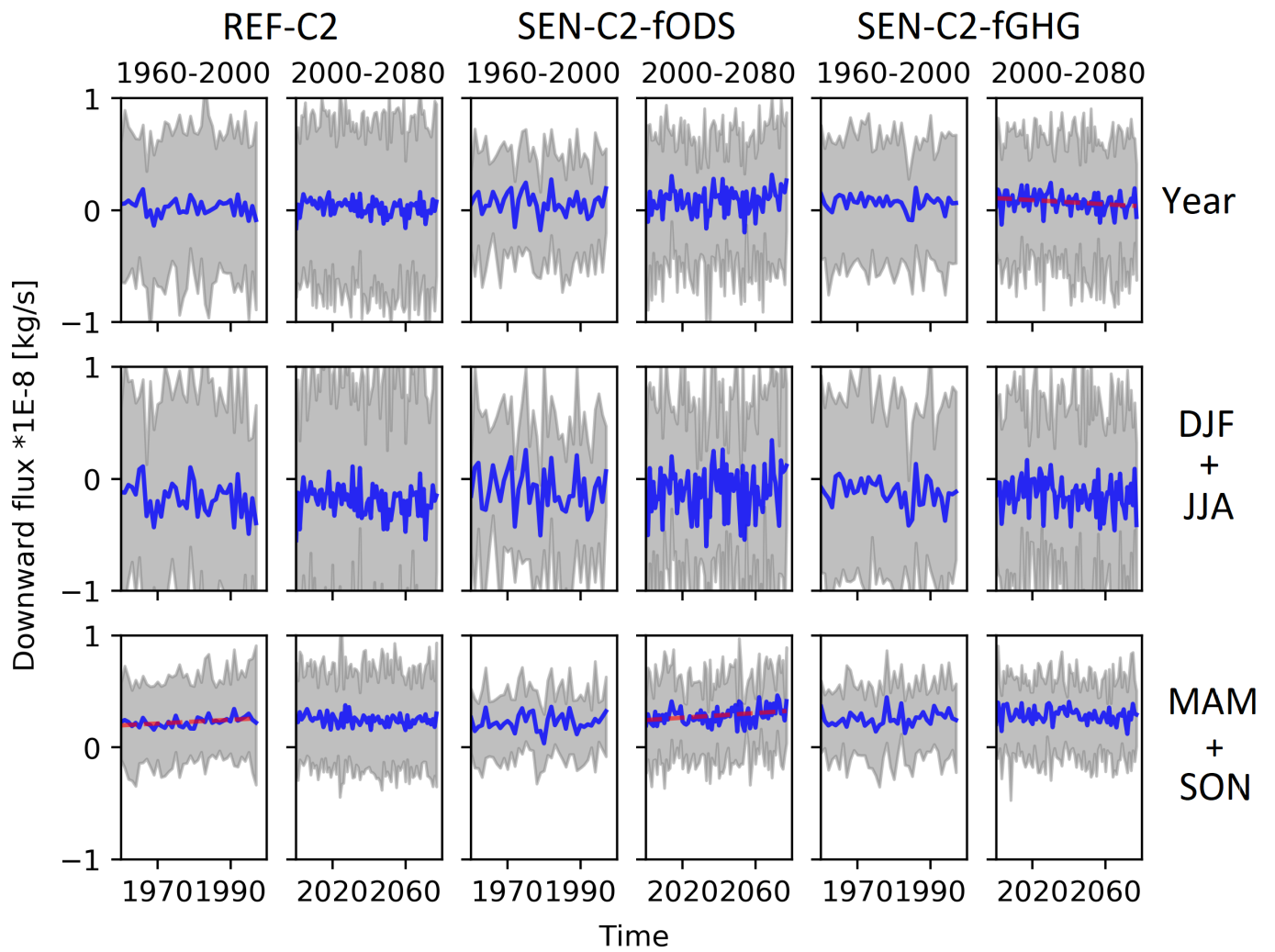
Figure 4.7: NH minus SH downward mass flux time lines.

4.3 Trends in Transport

The difference in vertical mass flux between the averages for the period 2040-2080 and 1960-2000 are shown in Fig. 4.8 for the REF-C2 scenario. We see that the differences roughly copy the climatology of Fig. 4.2, i.e. a positive change in upwelling and a negative change in downwelling, confirming the overall increase in circulation. Exceptions are certain areas in the tropics where we see a slightly negative change. This area is most pronounced for JJA (Fig. 4.8c) between 10 and 2 hPa.
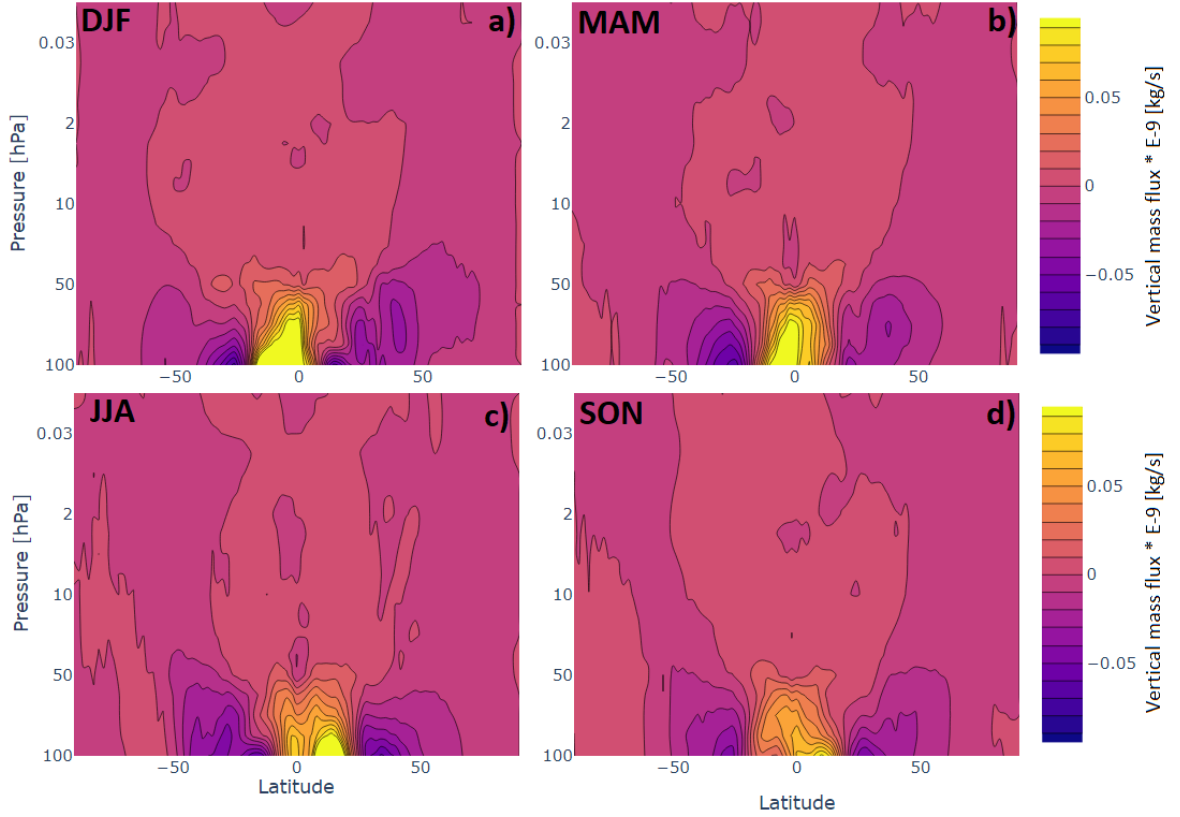
Figure 4.8: Seasonal mean vertical mass climatology change from 1960-2000 to 2040-2080 from REF-C2 scenario. Positive values denote upward motions.

The spatial distribution of trends compared to climatology at the stratopause is shown in Fig. 4.9. Trends for the REF-C2 and SEN-C2-fODS scenarios confirmed an increase in overall upwelling and downwelling. For SEN-C2-fGHG, the trends are generally smaller. The statistical significance of these trends has been calculated, but its values vary for individual latitudes and it is not possible to clearly illustrate the resulting statistical evaluation. Thus, in the figures of the spatial distribution of trends, we present the resulting values without indicating significance. The graphs then give rather a general idea of the geographical distribution of the changes in the transport across the stratopause than an illustration of the absolute values of these changes.

The trends corresponding to the time series in Fig. 4.4, 4.5 and 4.6 are summarised in Tab. 4.1, 4.2 and 4.3, together with the relative change compared with the 1960-2000 average. Tab. 4.1 shows trends in upward motions. We can see an annual increase in upwelling for both periods for the REF-C2 and SEN-C2-fODS scenarios (1.44%-1.68% over a decade). Except for JJA 1960-2000, all seasons for the REF-C2 scenario have a significant growing trend. The strongest growth is for SON 1960-2000, with a 2.83% increase over a decade. For the ODSs-fixed scenario, the only season with the significant trend for the 1960-2000 period is DJF, with a high increase of about 3% over a decade. For 2000-2080, all trends are statistically significant. Concerning the SEN-C2-fGHG scenario, the only significant trends are for summer and winter 2000-2080. However, these trends are relatively weak (less than 1% over a decade).
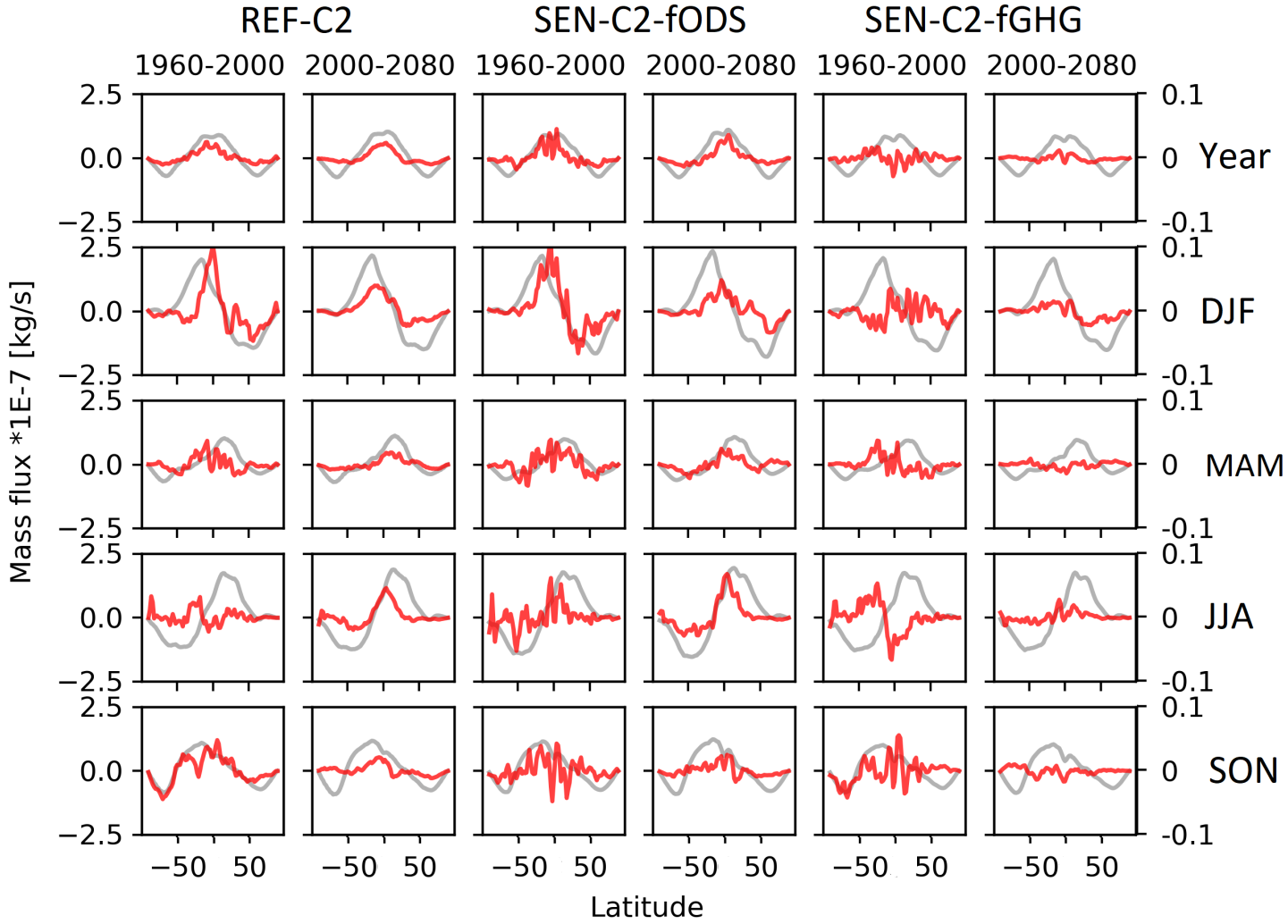
28

Figure 4.9: Spatial distribution of trends (red line) compared to climatology (gray line). The left axis is for climatology and the right for trends. Statistical significance of the trends is not depicted.

Considering downward movements (Tab. 4.2), the strongest trend was also detected for SON 1960-2000 for REF-C2 (3.2% over a decade). Again, JJA 1960-2000 is the only period without a significant trend for REF-C2. However, the increase is not as substantial here as with ascents. This is also confirmed for SEN-C2-fODS. For example, for DJF, there was a clear increase in upwelling for both periods, but no significant trend was detected for downwelling. For the scenario with fixed GHGs, the growth of descending movements is not apparent for a period other than DFJ 2000-2080, with a increase of 1.14% over a decade. For JJA 1960-2000, there is even an significant decreasing trend (-1.56% over a decade).

Table 4.1: Upwelling through the stratopause trends over a decade with standard error in 10^6 kg/s for 1960-2000 and 2000-2080. The percentages given represent the relative change over a decade relative to the 1960-2000 average. The values marked in red are statistically significant.

	REF-C2		SEN-C2-fODS		SEN-C2-fGHG	
	1960-2000	2000-2080	1960-2000	2000-2080	1960-2000	2000-2080
Year	3.68±0.57 1.61%	3.29±0.25 1.44%	3.73±0.90 1.64%	3.82±0.31 1.68%	0.33±0.66 0.15%	0.21±0.26 0.09%
DJF	6.79±2.43 1.74%	7.01±0.83 1.80%	11.74±2.29 2.96%	5.44±1.17 1.37%	-0.80±2.18 -0.21%	2.44±0.91 0.64%
MAM	2.68±0.96 1.33%	2.78±0.38 1.38%	3.29±1.55 1.61%	2.43±0.52 1.19%	-0.54±1.44 -0.28%	-0.66±0.47 -0.34%
JJA	0.07±2.51 0.02%	5.10±1.01 1.38%	3.54±4.01 0.90%	7.68±1.19 1.95%	-4.95±3.11 -1.31%	2.66±0.89 0.71%
SON	7.67±1.17 2.83%	2.21±0.43 0.82%	1.84±1.56 0.67%	2.86±0.58 1.04%	1.77±2.10 0.68%	-0.88±0.52 -0.34%

Table 4.2: Downwelling through the stratopause trends over a decade with standard error in 10^6 kg/s for 1960-2000 and 2000-2080. The percentages given represent the relative change over a decade relative to the 1960-2000 average. The values marked in red are statistically significant.

	REF-C2		SEN-C2-fODS		SEN-C2-fGHG	
	1960-2000	2000-2080	1960-2000	2000-2080	1960-2000	2000-2080
Year	-2.74±0.84 1.34%	-2.62±0.28 1.28%	-2.91±0.86 1.43%	-3.08±0.35 1.51%	-0.04±0.73 0.02%	-0.44±0.26 0.23%
DJF	-6.85±3.27 -1.91%	-4.15±0.94 1.15%	-8.24±4.25 2.26%	-3.19±1.79 0.88%	-1.18±2.67 0.33%	-4.04±1.22 1.14%
MAM	-2.27±0.99 1.35%	-2.39±0.34 1.42%	-3.16±1.42 1.61%	-2.22±0.46 1.32%	0.72±1.29 -0.45%	0.43±0.44 -0.27%
JJA	1.32±2.02 -0.41%	-2.43±0.80 0.77%	-2.98±3.06 0.87%	-5.10±0.93 1.50%	5.10±2.50 -1.56%	-1.53±0.82 0.47%
SON	-7.31±1.08 3.20%	-1.32±0.37 0.58%	-1.69±1.28 0.73%	-2.38±0.48 1.03%	-2.70±1.44 1.23%	0.85±0.45 -0.39%

The trends of total mass flux through the stratopause, shown in Tab. 4.3, reached relatively the highest values compared to the 1960-2000 average (over 10%). Nevertheless, many of these strong trends are burdened by a large statistical error and are not statistically significant. It is worth noting a comparison of the periods 1960-2000 and 2000-2080 for REF-C2 when no trend is significant for 1960-2000. In contrast, for the period 2000-2080, all trends are significant, with the maximum for DFJ (9.37% over a decade).

Table 4.3: Total mass flux through the stratopause trends over a decade with standard error in 10^6 kg/s for 1960-2000 and 2000-2080. The percentages given represent the relative change over a decade relative to the 1960-2000 average. The values marked in red are statistically significant.

	REF-C2		SEN-C2-fODS		SEN-C2-fGHG	
	1960-2000	2000-2080	1960-2000	2000-2080	1960-2000	2000-2080
Year	0.94±0.70	0.67±0.12	0.81±0.34	0.75±0.11	0.30±0.30	-0.24±0.11
	4.09%	2.92%	3.40%	3.12%	1.27%	-1.04%
DJF	-0.07±2.50	2.86±0.66	3.50±3.65	2.24±1.20	-1.98±2.13	-1.60±0.98
	-0.24%	9.37%	10.78%	6.91%	-7.25%	-5.85%
MAM	0.41 ± 0.25	0.39±0.11	0.12±0.36	0.21±0.12	0.18±0.32	-0.23±0.12
	1.23%	1.17%	0.34%	0.58%	0.54%	-0.69%
JJA	1.39±1.79	2.67±0.71	0.56±2.96	2.57±1.04	0.15±2.16	1.14±0.88
	2.57%	4.94%	1.05%	4.76%	-0.29%	2.24%
SON	0.35 ± 0.50	0.89±0.19	0.15±0.64	0.49±0.25	-0.93±1.00	-0.02±0.27
	0.84%	2.13%	0.35%	1.11%	-2.39%	-0.04%

Chapter 5

Discussion and Summary

The redistribution of ozone and other substances in the middle atmosphere is controlled by the large-scale BDC (Fig. 2.4). The residual stream function (Fig. 4.1) describes the BDC, as it contains information on the meridional and vertical motions of air masses. In this bachelor's thesis, we focused on vertical movements, especially vertical mass flux through the stratopause. The residual stream function data are based on chemistry-climatic models from the CCMI-1. We examined trends for the period 1960-2080 based on three different scenarios. Using the differences between these scenarios, it is possible to estimate the impact of GHGs and ODSs on the BDC changes.

At altitudes corresponding to the stratopause (about 1 hPa), the main driver of the transport is the BDC deep branch, occurring as a single circulation cell from the summer to winter pole. Its seasonal change is clearly visible in Fig. 4.3. The strongest circulation occurs in summer and winter when the radiation differences between the hemispheres are greatest. Transport has a different structure during MAM and SON, during which there are downward movements in both hemispheres at higher latitudes. In the tropics, there is upwelling with the maximum shifted towards the NH during MAM and towards the SH in SON. Figs. 4.3, 4.4 and 4.5 suggest that for the non-fixing GHGs scenarios, there is an intensification of the upward movements when comparing the periods 1960-1990 and 2050-2080. A weaker trend is also noticeable for downward movements. The unambiguous dependence of changes in circulation on GHGs was also confirmed for other results.

From previous analyses, we know that the deep branch of the BDC is stronger in the NH (Butchart, 2014). However, significant hemispheric differences in downward movements were not confirmed. In addition, no future changes in these differences were found. These findings are not necessarily excluded, as the height of the stratopause and air density also play a role in transport and may vary between hemispheres. Performing a deeper analysis of hemispheric differences in the future could shed more light on the effects of these factors.

The main result of this bachelor thesis is the analysis of integrated upward, downward and total mass flux through the stratopause. The seasonal changes of these movements correspond with a common understanding of the BDC, i.e. the strongest upward and downward movements during winter and summer and about half the flow during spring and autumn. To illustrate ongoing and anticipated the BDC changes, we have also analysed trends in the integrated transport. We have

assessed the periods 1960-2000 and 2000-2080 separately to detect potential influence in the ODS concentration trends. For the main analyzed REF-C2 scenario, a statistically significant increase in upward and downward mass flux was detected, with the exception of JJA 1960-2000 for all seasonal and annual averages. Average annual increases range between 1.28% and 1.61%. The strongest trend was detected for SON 1960-2000 (2.83% for upwelling and 3.20% for downwelling).

It seems that the circulation is being amplified, with the overall mass flux not changing much. This is true mainly for the period 1960-2000, when the total flow does not change significantly (first column in Tab. 4.3). However, the situation is different for the period 2000-2080. Considering REF-C2, all seasons recorded a significant increase in the total transport manifested as faster growth of the upwelling. For all scenarios, the total transport between the stratosphere and mesosphere is positive. This means that more matter flows from the stratosphere to the mesosphere than vice versa. A recent study (Pišoft et al., 2021) shows that the stratosphere is shrinking, which would be offered as a possible explanation. However, the shrinkage was only confirmed for the scenarios with non-fixed GHGs. Thus, the effect of the stratospheric shrinkage cannot be the only factor causing overall positive transport.

Assessing the influence of ODSs on the development of the BDC is relatively difficult. In contrast to GHGs, which appear to be important drivers of transport enhancements in the middle atmosphere, no dramatic difference was observed between the REF-C2 and SEN-C2-fODS scenarios. Although the trends differed significantly between these simulations for some seasons, it should be borne in mind that the results are affected by the different number of models involved, which differed for both scenarios (8 for REF-C2 and only 3 for SEN-C2-fODS). Thus, model variability comes into play, even though outliers have been detected.

A possible systematic error of the procedure using the residual stream function might be linked to the accuracy of the numerical derivative. A calculation based directly on residual vertical velocities multiplied by density could be more accurate. In the future, an analogous analysis based on direct calculation is planned.

Since there is no published scientific study on the topic of the transport between the stratosphere and mesosphere an its trends, we plan to extend this study, assess other details of related processes and the stratospheric shrinkage, and submit a paper based on the presented results.

Bibliography

H. Akiyoshi, T. Nakamura, T. Miyasaka, M. Shiotani, and M. Suzuki. A nudged chemistry-climate model simulation of chemical constituent distribution at northern high-latitude stratosphere observed by smiles and mls during the 2009/2010 stratospheric sudden warming. *Journal of Geophysical Research: Atmospheres*, 121(3):1361–1380, 2016. URL https://agupubs.onlinelibrary.wiley.com/doi/abs/10.1002/2015JD023334.

D. G. Andrews, J. R. Holton, and C. B. Leovy. *Middle atmosphere dynamics*. Academic Press, 1987.

T. Birner and H. Bönisch. Residual circulation trajectories and transit times into the extratropical lowermost stratosphere. *Atmospheric Chemistry and Physics*, 11(2):817–827, 2011. URL https://acp.copernicus.org/articles/11/817/2011/.

N. Butchart. The brewer-dobson circulation. *Reviews of Geophysics*, 52(2):157–184, 2014. URL https://agupubs.onlinelibrary.wiley.com/doi/abs/10.1002/2013RG000448.

M. Deushi and K. Shibata. Development of a meteorological research institute chemistry-climate model version 2 for the study of tropospheric and stratospheric chemistry. *Papers in Meteorology and Geophysics*, 62:1–46, 2011. URL https://www.jstage.jst.go.jp/article/mripapers/62/0/62_0_1/_article.

E. Dlugokencky and P. Tans. Trends in atmospheric carbon dioxide, 2021. URL https://www.esrl.noaa.gov/gmd/ccgg/trends/gl_data.html.

R. Eichinger and P. Šácha. Overestimated acceleration of the advective brewer–dobson circulation due to stratospheric cooling. *Quarterly Journal of the Royal Meteorological Society*, 146(733):3850–3864, 2020. URL https://rmets.onlinelibrary.wiley.com/doi/abs/10.1002/qj.3876.

J. C. Farman, B. G. Gardiner, and J. D. Shanklin. Large losses of total ozone in antarctica reveal seasonal clox/nox interaction. *Nature*, 315(6016):207–210, 1985.

R. Garcia, A. Smith, D. Kinnison, Á. de la Cámara, and D. J. Murphy. Modification of the gravity wave parameterization in the whole atmosphere community climate model: Motivation and results. *Journal of the Atmospheric Sciences*, 74(1):275 – 291, 2017. URL https://journals.ametsoc.org/view/journals/atsc/74/1/jas-d-16-0104.1.xml.

D.L. Hartmann. *Global physical climatology: Second Edition.* Elsevier, 2015.

M. I. Hegglin, D. W. Fahey, M. McFarland, S. A. Montzka, and E. R. Nash. Twenty questions and answers about the ozone layer: 2014 update. *World Meteorological Organization, UNEP, NOAA, NASA, and European Commission.*, 2014. URL https://csl.noaa.gov/assessments/ozone/2014/.

K. Imai, N. Manago, C. Mitsuda, Y. Naito, E. Nishimoto, T. Sakazaki, M. Fujiwara, L. Froidevaux, T. von Clarmann, G. P. Stiller, D. P. Murtagh, P. Rong, M.G. Mlynczak, K. A. Walker, D. E. Kinnison, H. Akiyoshi, T. Nakamura, T. Miyasaka, T. Nishibori, S. Mizobuchi, K. Kikuchi, H. Ozeki, C. Takahashi, H. Hayashi, T. Sano, M. Suzuki, M. Takayanagi, and M. Shiotani. Validation of ozone data from the superconducting submillimeter-wave limb-emission sounder (smiles). *Journal of Geophysical Research: Atmospheres*, 118(11): 5750–5769, 2013. URL https://agupubs.onlinelibrary.wiley.com/doi/abs/10.1002/jgrd.50434.

IPCC. *Summary for Policymakers*, book section SPM, page 1–30. Cambridge University Press, Cambridge, United Kingdom and New York, NY, USA, 2013. URL www.climatechange2013.org.

P. Jöckel, A. Kerkweg, A. Pozzer, R. Sander, H. Tost, H. Riede, A. Baumgaertner, S. Gromov, and B. Kern. Development cycle 2 of the modular earth submodel system (messy2). *Geoscientific Model Development*, 3(2):717–752, 2010. URL https://gmd.copernicus.org/articles/3/717/2010/.

P. Jöckel, H. Tost, A. Pozzer, M. Kunze, O. Kirner, C. A. M. Brenninkmeijer, S. Brinkop, D. S. Cai, C. Dyroff, J. Eckstein, F. Frank, H. Garny, K.-D. Gottschaldt, P. Graf, V. Grewe, A. Kerkweg, B. Kern, S. Matthes, M. Mertens, S. Meul, M. Neumaier, M. Nützel, S. Oberländer-Hayn, R. Ruhnke, T. Runde, R. Sander, D. Scharffe, and A. Zahn. Earth system chemistry integrated modelling (escimo) with the modular earth submodel system (messy) version 2.51. *Geoscientific Model Development*, 9(3):1153–1200, 2016. URL https://gmd.copernicus.org/articles/9/1153/2016/.

A. I. Jonsson, J. de Grandpré, V. I. Fomichev, J. C. McConnell, and S. R. Beagley. Doubled co2-induced cooling in the middle atmosphere: Photochemical analysis of the ozone radiative feedback. *Journal of Geophysical Research: Atmospheres*, 109(D24), 2004. URL https://agupubs.onlinelibrary.wiley.com/doi/abs/10.1029/2004JD005093.

D. Marsh, M. Mills, D. Kinnison, J. Lamarque, N. Calvo, and L. Polvani. Climate change from 1850 to 2005 simulated in cesm1(waccm). *Journal of Climate*, 26(19):7372 – 7391, 2013. URL https://journals.ametsoc.org/view/journals/clim/26/19/jcli-d-12-00558.1.xml.

V. Masson-Delmotte, P. Zhai, H.-O. Pörtner, D. Roberts, J. Skea, P.R. Shukla, A. Pirani, W. Moufouma-Okia, C. Péan, R. Pidcock, S. Connors, J.B.R. Matthews, Y. Chen, X. Zhou, M.I. Gomis, E. Lonnoy, T. Maycock, M. Tignor, and Waterfield T. . Ipcc, 2018: Global warming of 1.5°c. an ipcc special report

on the impacts of global warming of 1.5°c above pre-industrial levels and related global greenhouse gas emission pathways, in the context of strengthening the global response to the threat of climate change, sustainable development, and efforts to eradicate poverty. *World Meteorological Organization*, 2018. URL https://www.ipcc.ch/sr15/.

M. Meinshausen, S. Smith, K. Calvin, J. S. Daniel, M.. Kainuma, J-F. Lamarque, K. Matsumoto, S. Montzka, S. Raper, K. Riahi, A. Thomson, G. Velders, and D. van Vuuren. The rcp greenhouse gas concentrations and their extensions from 1765 to 2300. *Climatic Change*, 109(1-2):213–241, 2011. URL https://link.springer.com/article/10.1007%2Fs10584-011-0156-z.

K Mohanakumar. *Stratosphere troposphere interactions: An introduction.* Springer, 2008.

A. Molod, L. Takacs, M. Suarez, J. Bacmeister, I Song, and A Eichmann. The geos-5 atmospheric general circulation model: Mean climate and development from merra to fortuna. *Technical Report Series on Global Modeling and Data Assimilation*, 28:124, 12 2012. URL https://gmao.gsfc.nasa.gov/pubs/docs/tm28.pdf.

A. Molod, L. Takacs, M. Suarez, and J. Bacmeister. Development of the geos-5 atmospheric general circulation model: evolution from merra to merra2. *Geoscientific Model Development*, 8(5):1339–1356, 2015. doi: 10.5194/gmd-8-1339-2015. URL https://gmd.copernicus.org/articles/8/1339/2015/.

O. Morgenstern, P. Braesicke, F. M. O'Connor, A. C. Bushell, C. E. Johnson, S. M. Osprey, and J. A. Pyle. Evaluation of the new ukca climate-composition model – part 1: The stratosphere. *Geoscientific Model Development*, 2(1): 43–57, 2009. URL https://gmd.copernicus.org/articles/2/43/2009/.

O. Morgenstern, G. Zeng, N. L. Abraham, P. J. Telford, P. Braesicke, J. A. Pyle, S. C. Hardiman, F. M. O'Connor, and C. E. Johnson. Impacts of climate change, ozone recovery, and increasing methane on surface ozone and the tropospheric oxidizing capacity. *Journal of Geophysical Research: Atmospheres*, 118(2):1028–1041, 2013. URL https://agupubs.onlinelibrary.wiley.com/doi/abs/10.1029/2012JD018382.

O. Morgenstern, M. I. Hegglin, E. Rozanov, F. M. O'Connor, N. L. Abraham, H. Akiyoshi, A. T. Archibald, S. Bekki, N. Butchart, M. P. Chipperfield, M. Deushi, S. S. Dhomse, R. R. Garcia, S. C. Hardiman, L. W. Horowitz, P. Jöckel, B. Josse, D. Kinnison, M. Lin, E. Mancini, M. E. Manyin, M. Marchand, V. Marécal, M. Michou, L. D. Oman, G. Pitari, D. A. Plummer, L. E. Revell, D. Saint-Martin, R. Schofield, A. Stenke, K. Stone, K. Sudo, T. Y. Tanaka, S. Tilmes, Y. Yamashita, K. Yoshida, and G. Zeng. Review of the global models used within phase 1 of the chemistry-climate model initiative (ccmi). *Geoscientific Model Development*, 10(2):639–671, 2017. URL https://gmd.copernicus.org/articles/10/639/2017/.

G. Myhre, D. Shindell, F.-M. Bréon, W. Collins, J. Fuglestvedt, J. Huang, D. Koch, J.-F. Lamarque, D. Lee, B. Mendoza, T. Nakajima, A. Robock, G. Stephens, T. Takemura, and H. Zhang. *Anthropogenic and natural radiative forcing*, pages 659–740. Cambridge University Press, Cambridge, UK, 2013. URL https://www.cambridge.org/core/books/climate-change-2013-the-physical-science-basis/anthropogenic-and-natural-radiative-forcing/63EB1057C36890FEAA4269F771336D4D.

L. D. Oman, J. R. Ziemke, A. R. Douglass, D. W. Waugh, C. Lang, J. M. Rodriguez, and J. E. Nielsen. The response of tropical tropospheric ozone to enso. *Geophysical Research Letters*, 38(13), 2011. URL https://agupubs.onlinelibrary.wiley.com/doi/abs/10.1029/2011GL047865.

L. D. Oman, A. R. Douglass, J. R. Ziemke, J. M. Rodriguez, D. W. Waugh, and J. E. Nielsen. The ozone response to enso in aura satellite measurements and a chemistry-climate simulation. *Journal of Geophysical Research: Atmospheres*, 118(2):965–976, 2013. URL https://agupubs.onlinelibrary.wiley.com/doi/abs/10.1029/2012JD018546.

G. Pitari, E. Di Genova, G.and Mancini, D. Visioni, I. Gandolfi, and I. Cionni. Stratospheric aerosols from major volcanic eruptions: A composition-climate model study of the aerosol cloud dispersal and e-folding time. *Atmosphere*, 7 (6), 2016. URL https://www.mdpi.com/2073-4433/7/6/75.

P. Pišoft, P. Šácha, Lorenzo M. Polvani, J. A. Añel, L de la Torre, R. Eichinger, U. Foelsche, P. Huszar, Ch. Jacobi, J. Karlický, A. Kuchař, J. Mikšovský, M. Žák, and H. E. Rieder. Stratospheric contraction caused by increasing greenhouse gases. *Environmental Research Letters*, 2021. URL http://iopscience.iop.org/article/10.1088/1748-9326/abfe2b.

R. A. Plumb. Stratospheric transport. *Journal of the Meteorological Society of Japan. Ser. II*, 80(4B):793–809, 2002. URL https://www.jstage.jst.go.jp/article/jmsj/80/4B/80_4B_793/_article.

L. E. Revell, F. Tummon, A. Stenke, T. Sukhodolov, A. Coulon, E. Rozanov, H. Garny, V. Grewe, and T. Peter. Drivers of the tropospheric ozone budget throughout the 21st century under the medium-high climate scenario rcp 6.0. *Atmospheric Chemistry and Physics*, 15(10):5887–5902, 2015. URL https://acp.copernicus.org/articles/15/5887/2015/.

J. F. Scinocca, N. A. McFarlane, M. Lazare, J. Li, and D. Plummer. Technical note: The cccma third generation agcm and its extension into the middle atmosphere. *Atmospheric Chemistry and Physics*, 8(23):7055–7074, 2008. URL https://acp.copernicus.org/articles/8/7055/2008/.

S. Solomon, D. Kinnison, J. Bandoro, and R. Garcia. Simulation of polar ozone depletion: An update. *Journal of Geophysical Research: Atmospheres*, 120 (15):7958–7974, 2015. URL https://agupubs.onlinelibrary.wiley.com/doi/abs/10.1002/2015JD023365.

A. Stenke, M. Schraner, E. Rozanov, T. Egorova, B. Luo, and T. Peter. The socol version 3.0 chemistry–climate model: description, evaluation, and implications from an advanced transport algorithm. *Geoscientific Model Development*, 6 (5):1407–1427, 2013. URL https://gmd.copernicus.org/articles/6/1407/2013/.

K. A. Stone, O. Morgenstern, D. J. Karoly, A. R. Klekociuk, W. J. French, N. L. Abraham, and R. Schofield. Evaluation of the access – chemistry–climate model for the southern hemisphere. *Atmospheric Chemistry and Physics*, 16(4):2401–2415, 2016. URL https://acp.copernicus.org/articles/16/2401/2016/.

D. Visioni, G. Pitari, G. di Genova, S. Tilmes, and I. Cionni. Upper tropospheric ice sensitivity to sulfate geoengineering. *Atmospheric Chemistry and Physics*, 18(20):14867–14887, 2018. URL https://acp.copernicus.org/articles/18/14867/2018/.

World Meteorological Organization WMO. Meteorology a three-dimensional science: Second session of the commission for aerology. *WMO Bulletin*, 6(4): 136–137, 1957. URL https://library.wmo.int/index.php?lvl=notice_display&id=18807#.YHb4-EVR1PZ.

World Meteorological Organization WMO. Scientific assessment of ozone depletion: 2010. 2011. URL https://csl.noaa.gov/assessments/ozone/2010/.

World Meteorological Organization WMO. Scientific assessment of ozone depletion: 2018, global ozone research and monitoring project – report no. 58, 588 pp. 2018. URL https://csl.noaa.gov/assessments/ozone/2018/.

World Meteorological Organization WMO. Wmo greenhouse gas bulletin (ghg bulletin) - no. 16: The state of greenhouse gases in the atmosphere based on global observations through 2019. 2020. URL https://library.wmo.int/index.php?lvl=notice_display&id=21795#.YHmTN9JR1PY.

S. Yukimoto, Y. Adachi, M. Hosaka, T. Sakami, H. Yoshimura, M. Hirabara, T. Y. Tanaka, E. Shindo, H. Tsujino, M. Deushi, R. Mizuta, S. Yabu, A. Obata, H. Nakano, T. Koshiro, T. Ose, and A. Kitoh. A new global climate model of the meteorological research institute: Mri-cgcm3 mdash;model description and basic performancemdash;. *Journal of the Meteorological Society of Japan. Ser. II*, 90A:23–64, 2012. URL https://www.jstage.jst.go.jp/article/jmsj/90A/0/90A_2012-A02/_article.

List of Figures

List of Tables